

AN ALGORITHM FOR THE EXTRACTION OF OCEAN  
WAVE INFORMATION FROM BISTATIC HF  
GROUNDWAVE RADAR DATA - A SIMULATION

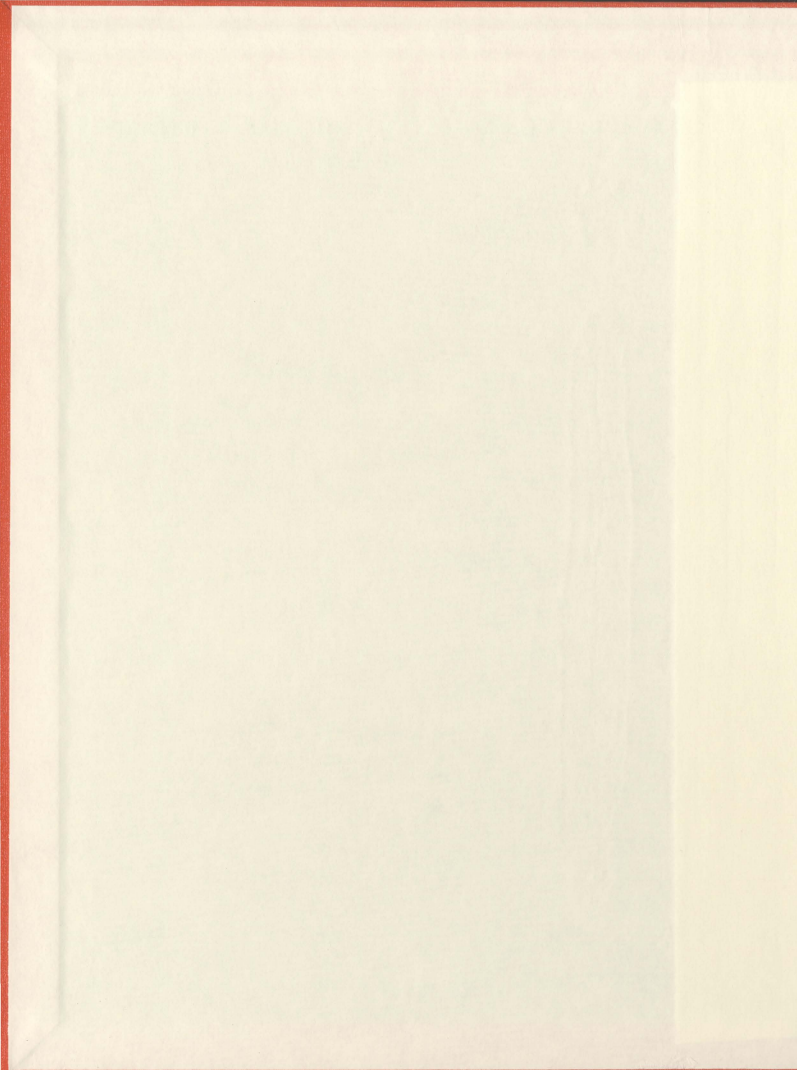
CENTRE FOR NEWFOUNDLAND STUDIES

---

**TOTAL OF 10 PAGES ONLY  
MAY BE XEROXED**

(Without Author's Permission)

JIANJUN ZHANG





# An Algorithm for the Extraction of Ocean Wave Information from Bistatic HF Groundwave Radar Data — A Simulation

by



©Jianjun Zhang, B.Eng

A thesis submitted to the School of Graduate Studies  
in partial fulfillment of the requirements for the  
degree of Master of Engineering

Faculty of Engineering and Applied Science  
Memorial University of Newfoundland  
November, 2003

St. John's

Newfoundland

# Abstract

In this thesis an algorithm is developed for the inverse problem of bistatic scattering from the ocean surface. Narrow beam bistatic high frequency (HF) radar data from the ocean surface are simulated and the non-directional ocean wave spectrum is recovered. The water depth is set to be arbitrary. Zero-mean Gaussian noise from external sources is taken into account.

The bistatic HF radar cross sections are applied to the general-depth water case. The second-order cross section of patch scattering is a two-dimensional Fredholm-type integral equation of first kind. It contains a non-linear product of ocean wave directional spectrum factors in its integrand. The energy inside the first-order cross section is derived to normalize this integrand. The unknown ocean wave spectrum is represented by truncated Fourier series. The integral equation is then converted to a matrix equation and a singular value decomposition (SVD) method is invoked to pseudo-invert the kernel matrix. The non-directional ocean wave spectrum is obtained from the Fourier coefficient  $a_0$ .

The zero-mean Gaussian noise from external sources is added to simulate pulsed HF radar clutter from the ocean surface. The power spectral densities of the clutter and noise are obtained by means of a periodogram. The combination of power spectral densities of clutter and noise makes the simulated bistatic radar data correspond more closely with actual observations. The inverse algorithm is carried out with respect to radar data for varying water depths, wind velocities, and radar operating frequencies. The results are compared with the original ocean wave spectrum.

# Acknowledgements

The author wishes to express his sincerest thanks to the Faculty of Engineering and Applied Science for affording him the opportunity of conducting this work. Particularly, the suggestions and guidance of the author's supervisor, Dr. Eric Gill, are greatly appreciated.

Thanks are also owed to author's colleagues and friends, Pradeep Bobby and Feng Liang, for their help and assistance on computer programming and other aspects at various stages of the work.

The work could not have been completed without the graduate student support from a Natural Science and Engineering Research Council (NSERC) grant to Dr. Eric Gill.

The patience and understanding of the author's wife and family are also appreciated.

# Contents

Abstract

Acknowledgements

Contents

List of Figures

List of Tables

Table of Symbols

<b>1</b>	<b>Introduction</b>	<b>1</b>
1.1	General Introduction . . . . .	1
1.2	Literature Review . . . . .	3
1.3	Scope of the Thesis . . . . .	9
<b>2</b>	<b>Calculation of the Bistatic Cross Sections</b>	<b>11</b>
2.1	General . . . . .	11
2.2	Calculation of the First-order Cross Section . . . . .	20
2.3	Calculation of the Second-order Cross Section . . . . .	23
2.3.1	Normalized Version of Second-order Cross Section . . . . .	23
2.3.2	The Solution of the Delta Function Constraint . . . . .	27
2.3.3	The Choice of a Directional Ocean Wave Spectrum . . . . .	29

<b>3</b>	<b>Inversion of the Integral Equation</b>	<b>41</b>
3.1	General . . . . .	41
3.2	Selection of the Ocean Wavenumber Range . . . . .	42
3.3	The Linearization Method . . . . .	44
3.4	Discretization of the Integral Equation . . . . .	48
3.5	SVD Solution of the Matrix Equation . . . . .	51
3.6	Illustration of the Results . . . . .	54
	3.6.1 Recovery of Ocean Wave Spectra . . . . .	54
	3.6.2 Normalized RMS Waveheight . . . . .	57
<b>4</b>	<b>Inverse Analysis for Noisy Spectra</b>	<b>62</b>
4.1	General Introduction . . . . .	62
4.2	The PSD of Ocean Clutter . . . . .	63
4.3	The PSD of Stationary Gaussian Noise . . . . .	65
4.4	The Time Series of Radar Return and its PSD . . . . .	67
4.5	The Inverse Analysis for Noisy Spectra . . . . .	73
	4.5.1 Recovery of Ocean Wave Spectra . . . . .	73
	4.5.2 Normalized RMS Waveheight . . . . .	73
<b>5</b>	<b>Conclusions</b>	<b>79</b>
5.1	General Summary . . . . .	79
5.2	Suggestions for Future Work . . . . .	80
<b>A</b>	<b>Computer Programs for Analysis</b>	<b>86</b>

# List of Figures

1.1	The simulated bistatic first- and second-order cross sections of the patch scatter. Wind speed is 15m/s, wind direction is $0^\circ$ , bistatic angle is $30^\circ$ . . . . .	4
2.1	The geometrical relationship of the bistatic configuration. . . . .	13
2.2	The two sections of the bistatic first-order cross section. . . . .	15
2.3	An enlarged view of the second-order scattering wave vectors for the bistatic patch scatter. . . . .	16
2.4	The four sections of the bistatic second-order cross section. Only $K_1 < K_2$ case is denoted here. . . . .	17
2.5	The combination of bistatic first- and second-order cross sections of the patch scatter. The radar operating frequency is 25 MHz, wind speed is 15m/s, wind direction is $0^\circ$ , and bistatic angle is $30^\circ$ . . . . .	32
2.6	The geometry of bistatic patch scatter. The ellipse normal is $90^\circ$ . Wind direction is indicated against the $x$ -axis, Bistatic angle is $30^\circ$ . . . . .	35
2.7	Bistatic second-order cross sections for water in different depths. The bistatic angle is $\phi_0 = 30^\circ$ . The wind velocity is 15 m/s, $0^\circ$ to the $x$ -axis. The radar operating frequency is 25 MHz. . . . .	36
2.8	Bistatic second-order cross sections for a wind speed of 15 m/s and wind directions of $\theta_w = 0^\circ, 45^\circ, 90^\circ$ , and $135^\circ$ . The radar operating frequency is 25 MHz. Deep water is assumed. . . . .	37

2.9	Bistatic second-order cross sections for wind speed in 10 m/s. The other parameters are kept consistent with Figure 2.8. Comparison of these two figures indicates the difference of the magnitude of the second-order cross sections. . . . .	38
2.10	Bistatic second-order cross sections for radar operating frequencies are 25 MHz, 10 MHz, and 5.75 MHz. Wind speed is 15 m/s, deep water, the wind direction is parallel the reference direction. . . . .	39
2.11	The cross sections for bistatic angles $0^\circ$ (monostatic) and $30^\circ$ . Wind speed is 15 m/s, the radar operating frequency is 25 MHz, deep water, the wind direction is $0^\circ$ to the $x$ -axis. . . . .	40
3.1	A example of the choice of the retained number of singular values. The rank of the kernel matrix is located by a "*" with a value of $r = 172$ . The radar frequency is 25 MHz. The wind speed is 15 m/s and the wind direction is zero degrees to the $x$ -axis. . . . .	53
3.2	Comparison of spectra from inversion (solid line) with Pierson-Moskowitz model (dashed line) for different water depths. Radar frequency is 25 MHz. The wind speed is 15 m/s and the wind direction is $0^\circ$ to the $x$ -axis. . . . .	55
3.3	Comparison of spectra from inversion (solid line) with Pierson-Moskowitz model (dashed line) for different wind directions. The water is deep. The radar frequency is 25 MHz. The wind speed is 15 m/s. . . . .	56
3.4	Comparison of spectra from inversion (solid line) with Pierson-Moskowitz model (dashed line) for different wind directions. The water is deep. The radar frequency is 25 MHz. The wind speed is 10 m/s. . . . .	58
3.5	Comparison of spectra from inversion (solid line) with Pierson-Moskowitz model (dashed line) for different radar frequencies. The water is deep. The wind speed is 15 m/s and the wind direction is $0^\circ$ to the $x$ -axis. . . . .	59

4.1 A pulse train with pulse width  $\tau_0$  and pulse repetition frequency  $T_L$ .  $n_0$  is the noise. . . . . 64

4.2 The simulated radar Doppler power spectral density (PSD) with zero-mean stationary Gaussian noise for water at different depths. The bistatic angle is  $\phi_0 = 30^\circ$ , the wind velocity is 15 m/s,  $0^\circ$  to the  $x$ -axis; the radar operating frequency is 25 MHz. . . . . 69

4.3 The simulated radar Doppler power spectral density (PSD) with zero-mean stationary Gaussian noise for wind speed of 15 m/s. The wind directions are  $\theta_w = 0^\circ, 45^\circ, 90^\circ$ , and  $135^\circ$ . The radar operating frequency is 25 MHz, bistatic angle is  $30^\circ$ , and deep water is assumed. Since  $45^\circ$  and  $135^\circ$  are symmetric with respect to the ellipse normal, we cannot tell the difference between them. . . . . 70

4.4 The simulated radar Doppler power spectral density (PSD) with zero-mean stationary Gaussian noise for a wind speed of 10 m/s. The other parameters are kept consistent with Figure 4.3. Comparison of these two figures indicates the difference of the magnitude of the second-order cross sections. 71

4.5 The simulated radar Doppler power spectral density (PSD) with different radar operating frequencies. Wind speed: 15 m/s, wind direction:  $0^\circ$  to  $x$ -axis, bistatic angle:  $30^\circ$ , and deep water. . . . . 72

4.6 The recovered non-directional spectra from noisy radar Doppler PSD for different water depths. Radar frequency is 25 MHz, the wind speed is 15 m/s and the wind direction is zero degree to the  $x$ -axis. The solid lines are the wave spectra from inversion. The dashed lines are the spectra calculated by Pierson-Moskowitz model. . . . . 74

4.7	The recovered non-directional spectra from noisy radar Doppler PSD for different wind directions. The water is deep, the radar frequency is 25 MHz, and wind speed is 15 m/s. The solid lines are the wave spectra from inversion. The dashed lines are the spectra calculated by Pierson-Moskowitz model. . . . .	75
4.8	The recovered non-directional spectra from noisy radar Doppler PSD for different wind directions. The water is deep, the radar frequency is 25 MHz, and the wind speed is 10 m/s. The solid lines are the wave spectra from inversion. The dashed lines are the spectra calculated by Pierson-Moskowitz model. . . . .	76
4.9	The recovered non-directional spectra from noisy radar Doppler PSD for different radar frequencies. The wind speed is 15 m/s, wind direction is $0^\circ$ to $x$ -axis, bistatic angle is $30^\circ$ , and the water is deep. The solid lines are the wave spectra from inversion. The dashed lines are the spectra calculated by Pierson-Moskowitz model. . . . .	77

# List of Tables

3.1	Normalized Waveheights for Different Water Depths. . . . .	60
3.2	Normalized Waveheights for Different Wind Directions ( $\mu = 15$ m/s). . .	61
3.3	Normalized Waveheights for Different Wind Directions ( $\mu = 10$ m/s). . .	61
3.4	Normalized Waveheights for Different Radar Frequencies. . . . .	61
4.1	Normalized Waveheights for Different Water Depths. . . . .	78
4.2	Normalized Waveheights for Different Wind Directions ( $\mu = 15$ m/s). . .	78
4.3	Normalized Waveheights for Different Wind Directions ( $\mu = 10$ m/s). . .	78
4.4	Normalized Waveheights for Different Radar Frequencies. . . . .	78

## Table of Symbols

- $\omega_B$  : Doppler radian frequency of Bragg peaks (P. 5).
- $g$  : Acceleration due to gravity (P. 5).
- $k_0$  : Radar radiation wavenumber (P. 5).
- $\phi_0$  : Bistatic angle (P. 5).
- $\sigma_1$  : First-order bistatic cross section (P. 5).
- $\sigma_{2P}$  : Second-order bistatic cross section of patch scatter (P. 5).
- $\sigma_{2T}$  : Second-order bistatic cross section with one of scatters occurs at the ocean surface near the radar transmitter (P. 5).
- $\sigma_{2R}$  : second-order bistatic cross section with one of scatters occurs at the ocean surface near the radar receiver (P. 5).
- $\sigma_{Total}$  : The total radar cross section of the ocean surface (P. 6).
- $\eta$  : Normalized Doppler frequency (P. 8).
- $K$  : Ocean wavenumber (P. 11).
- $d$  : Water depth (P. 11).
- $\hat{N}$  : Unit normal to the scattering ellipse (P. 13).
- $\theta_N$  : Direction of  $\hat{N}$  (P. 13).
- $\vec{K}$  : The scattering wave vector (P. 14).
- $S_1(m\vec{K})$  : The directional wave spectrum (P. 14).
- $\Delta\rho_s$  : The scattering patch width (P. 14).
- $Sa(\cdot)$  : Sampling function (P. 14).
- $c$  : Free space speed of light ( $= 3 \times 10^8$  m/s) (P. 14).
- $\tau_0$  : Pulse width in time (P. 14).
- $\delta(\cdot)$  : Dirac delta function (P. 15).

- ${}_S\Gamma_P$  : Symmetric coupling coefficient (P. 15).
- $P_1, P_2, P_3,$  and  $P_4$  : The four parts of the second-order cross section from left to right (P. 16).
- ${}_H\Gamma_P$  : Hydrodynamic coupling coefficient (P. 18).
- ${}_E\Gamma_p$  : Electromagnetic coupling coefficient (P. 18).
- $K_{Bmono}$  : Bragg peak wavenumber for monostatic scattering ( $K_{Bmono} = 2k_0$ ) (P. 20).
- $\vec{K}_n$  : Normalized wave vector (P. 21).
- $K_n$  : Normalized wavenumber (P. 21).
- $D$  : Normalized water depth (P. 21).
- $Z(\cdot)$  : Normalized ocean wave spectrum (P. 22).
- $\sigma_{1n}(\eta)$  : Normalized first-order cross section (P. 22).
- $E_{m1}$  : Energy inside the first-order cross section (P. 22).
- $\Gamma_n$  : Normalized coupling coefficients (P. 23).
- $\sigma_{2n}(\eta)$  : Normalized second-order cross section (P. 24).
- $J_{tn} = \left| \frac{\partial Y_n}{\partial D_p} \right|$  : Normalized Jacobian transformation (P. 26).
- $g(\theta_{\vec{K}})$  : Normalized directional distribution (P. 29).
- $S_{PM}(K)$  : Pierson-Moskowitz spectrum (P. 30).
- $s(K)$  : Spread function (P. 30).
- $\bar{\theta}(K)$  : mean wind direction (P. 30).
- $\Gamma$  : Gamma function (P. 31).
- $F_B$  : first-order peak denoted on Figure 2.5 (P. 32).
- $J_s$  : Singularities from Jacobian transformation for Figure 2.5 (P. 32).
- $\mu$  : The magnitude of normalized Doppler frequency shift from the first-order peaks (P. 42).
- $K_{1L}$  : The lower limitations of the wavenumber band (P. 43).
- $K_{1U}$  : The upper limitations of the wavenumber band (P. 43).

- $F_p$  : Phillips equilibrium spectrum (P. 44).
- $a_n$  : Coefficients of Fourier series ( $n = 0, 1, 2, \dots$ ) (P. 44).
- $\sigma_{2pmL}(\eta)$  : The linearized version of the second-order cross section of patch scattering (P. 45).
- $\alpha^*$  : The dominant direction of the wavefield (P. 47).
- $\underline{\underline{C}}$  : The kernel matrix equation (P. 49).
- $\underline{X}$  : A column array with its elements as the Fourier coefficients corresponding for each wave frequency band (P. 49).
- $\underline{B}$  : A column array with its elements being the simulated radar data selected for inversion (P. 49).
- $\underline{\underline{C}}^{-1}$  : The inverse of kernel matrix  $\underline{\underline{C}}$  (P. 51).
- $\underline{\underline{C}}^+$  : Pseudo-inverse matrix of  $\underline{\underline{C}}$  (P. 51).
- $\underline{U}$  : The right singular vectors of  $\underline{\underline{C}}$  (P. 52).
- $\underline{V}$  : The left singular vectors of  $\underline{\underline{C}}$  (P. 52).
- $H$  : normalized *rms* waveheight (P. 60).
- $f_0$  : Radar operating frequency (P. 63).
- $P_t$  : Transmitter peak power (P. 63).
- $G_t$  : Radar transmitter gain (P. 63).
- $d_s$  : Element space of receive array (P. 63).
- $BW_{\frac{1}{2}}$  : The half-power beam width (P. 63).
- $G_r$  : Receive array gain (P. 63).
- prf : The pulse repetition frequency (P. 64).
- $A_r$  : patch area (P. 64).
- $F(\cdot)$  : Rough spherical earth attenuation function (P. 64).
- $P_c$  : Doppler power spectral density of gated ocean clutter signal (P. 65).
- $P_N$  : Noise power spectral density (P. 65).

- $S_N(\omega')$  : Power spectral density of the ambient noise as a function of radian frequency,  $\omega'$  (P. 65).
- $f_a$  : External noise factor (P. 65).
- $k = 1.38 \times 10^{-23} J/K$  : Boltzmann's constant (P. 66).
- $T_0 = 290K$  : The reference temperature (P. 66).
- $B_n$  : The noise power bandwidth of the receiving system (P. 66).
- $F_{am}$  : External noise *figure* (P. 66).
- $B$  : Receiver bandwidth (P. 67).
- $f(t)$  : The time series of ocean wave signal (P. 67).
- $s(t)$  : The time series of "real-like" signal (P. 67).
- $c(t)$  : Gated ocean clutter signal (P. 67).
- $n(t)$  : Noise voltage as observed by a pulse radar (P. 67).

# Chapter 1

## Introduction

### 1.1 General Introduction

The increasing interest and importance in offshore development, search and rescue, defense, and scientific research require efficient and accurate measurements of the ocean surface conditions. Some parameters, such as directional wave spectra and wind fields, are critical for ocean investigation but not easily extracted using conventional oceanographic instruments. However, radio techniques for remote sensing provide a good means of meeting this challenge.

There are three main radio oceanographic techniques for the measurements of the ocean surface. They are microwave radiometry, microwave radar, and high frequency (HF) radar. Shearman[1] gives a good introduction to the remote sensing of the ocean surface by radio techniques. Among them, HF ground wave radar is of interest to the present thesis.

Operating in the HF electromagnetic wave band (3 MHz to 30 MHz), HF ground wave radar has the potential for sensing ocean surface parameters to ranges exceeding 200 km from the coastline. The transmitted radar signals, which are guided by a good conducting medium like ocean water, travel along the earth's curvature, reach far beyond the line-of-

sight horizon, and couple strongly with the ocean surface. The returning signals contain a large amount of information on ocean currents, waves, and winds.

HF radar waves interact strongly with ocean waves because their wavelengths are of the same order. The ocean waves in this wavelength range carry a large amount of wave spectral energy. The velocity of the ocean waves generally cause Doppler shifts on the incident radar carrier frequency. Typically, the resulting Doppler radar spectra are characterized by two significant "first-order" peaks surrounded by a higher order continuum. The procedure of extracting ocean wave information from the Doppler spectrum is referred to here as the inverse analysis, while the calculation of radar Doppler spectra from a corresponding model of the directional ocean wave spectrum is denoted as the forward analysis.

HF radar may be operated in monostatic or bistatic modes. A monostatic configuration means the radar transmitter and receiver are in the same location, while in a bistatic configuration the radar transmitter and receiver are located separately. Compared with a monostatic configuration, a bistatic configuration possesses some advantages in practical utilization. For instance, it is possible to use one full monostatic radar system in combination with a single separated receiver, rather than two separated monostatic radar systems, to obtain the wave directional information.

In this thesis, an algorithm is developed to implement the inverse analysis. The non-directional spectrum is obtained from ocean scatter received by an HF narrow beam radar operating bistatically. The HF second-order radar cross section of the ocean surface is described by a two-dimensional integral equation of the first kind. The integrand of the equation is normalized, linearized, discretized, and Fourier-represented to form a matrix equation. A singular value decomposition (SVD) method is invoked to invert the kernel matrix in the equation and the ocean wave information is recovered from the solution of the equation.

## 1.2 Literature Review

Ocean wave measurement by means of HF radar finds its roots in the explanation of the physical mechanism of Bragg scatter. Crombie [2] found that the discrete frequency shifts above and below the carrier frequency observed in the radar spectrum corresponded uniquely with ocean waves that have the wavelengths exactly one-half the radar operating wavelength if grazing incidence is assumed, and moving toward or away from the radar. The relative movement of water waves and the radar waves are mapped to the Doppler shift of the radar waves and may be expressed as the Doppler spectrum.

Since the signal scattered from the ocean surface is influenced by radar frequency, beam width, polarization, and configuration (monostatic or bistatic), the scattering cross section should be developed to explain the mechanism of the “radar wave-ocean wave” interaction. The radar cross section is defined as “that area which, when multiplied by the power flux density of the incident wave, would yield sufficient power that could produce by isotropic radiation, the same radiation intensity as that in a given direction from the scattering surface” [3].

Figure 1.1 depicts the first- and second-order cross sections when the wind direction is perpendicular to the radar beam. In this case, the first-order peaks, Bragg peaks, are equal in magnitude. In the figure, underlying currents are assumed to be absent. The second-order continuum is separated into two symmetric parts having positive and negative Doppler shifts surrounding the first-order peaks.

The derivation of the HF radar cross section for the ocean began initially with Barrick [4]. He extended Rice's [5] perturbation theory to develop a first-order scattering cross section which was seen to support Crombie's conjecture of Bragg scattering. In the same year, Barrick [6] derived a theoretical formulation for the second-order backscatter cross section which explained the continuum surrounding the first-order peaks. This formulation is a nonlinear, two-dimensional, Fredholm-type integral equation, in which

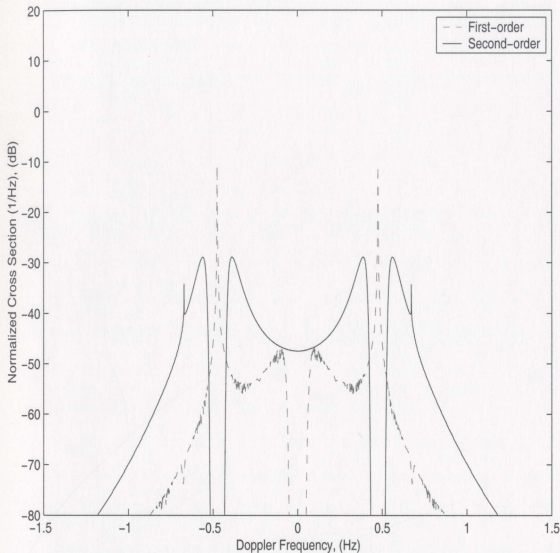


Figure 1.1: The simulated bistatic first- and second-order cross sections of the patch scatter. Wind speed is 15m/s, wind direction is  $0^\circ$ , bistatic angle is  $30^\circ$ .

the integrand contains the second-order electromagnetic and hydrodynamic coupling coefficients corresponding to the different mechanisms of interaction between radar signal and water waves. The nonlinear factor in the integrand arises from the product of two ocean wave directional spectra. A delta function in the integrand constrains the manner in which wave vectors from each of the two spectra must be related to produce the continuum referred to above.

Barrick and Lipa [7] further derived a set of expressions to account for shallow water. All of these models are for backscatter returns. Assumptions are made of grazing

incidence and vertical polarization of the radar wave.

Based upon Walsh's generalized-function approach [8], Srivastava [9] developed the first- and second-order monostatic cross sections in an alternative way. Srivastava's second-order cross section contains three parts. The first part is equivalent to Barrick's model and is denoted as the patch scatter term. The second-order on-patch scatter means the first and second scatters occur at a region that is far from the radar station. The other parts can be viewed as the interaction of the transmitting source with the surrounding ocean surface. The on-patch term is dominant among the three parts.

Walsh *et al.* [10] derived the third-order cross section. They found that the third-order cross section might be neglected in the region near the first-order peaks. However, the third-order cross section is important for the spectrum far from the first-order peaks and may not be overlooked if the analysis is in this region.

As the most recent progress in the development of HF radar cross section of the ocean surface, Gill and Walsh [11] presented bistatic first- and second-order radar cross sections using the generalized-function approach [8].

In [12], the first-order bistatic cross section,  $\sigma_1$ , contains a squared sampling function to model the first-order peaks. The locations of the first-order (or Bragg) peaks are at Doppler radian frequencies of  $\omega_B = \pm\sqrt{2gk_0 \cos(\phi_0)}$  if deep water is assumed. Here  $g$  is the acceleration due to gravity,  $k_0$  is the radiation wavenumber, and  $\phi_0$  is the bistatic angle defined as one-half of the angle between radar transmitter and receiver as viewed from the scattering point. The second-order bistatic cross section contains three parts. They are (1) the patch scattering, in which two scatters occur at the ocean surface far from the transmitter and receiver, (2) scattering in which one of two scatters occurs at the ocean surface near the radar transmitter, and (3) scattering in which one of the scatters is near the receiver. These three parts are signified in [12] as  $\sigma_{2P}$ ,  $\sigma_{2T}$ , and  $\sigma_{2R}$ , respectively. In each of the latter two cases, a second scatter occurs far from the radar

site. The total radar cross section,  $\sigma_{Total}$ , of the ocean surface without considering the third- and higher-order cases, contain four components: one first-order portion and the three second-order components.

$$\sigma_{Total} = \sigma_1 + \sigma_{2P} + \sigma_{2T} + \sigma_{2R} . \quad (1.1)$$

Among the three components of the second-order, the patch scattering  $\sigma_{2P}$  is dominant and will be treated in the inverse analysis.

Another significant achievement of Gill's work [12] is the consideration of external noise in the radar returns. Based upon the assumption of a pulsed radar system and characteristics of the external noise, a model for the ocean clutter signal to noise ratio is presented. The power spectral densities of clutter and noise are each converted to the time domain. The time series are combined and the resulting time-domain signal is Fourier transformed in order to obtain an estimation of the total power spectral density.

The development of the radar cross section leads to applications for the detection of the ocean wave parameters from the radar data. As previously mentioned, the required procedure is denoted as the inverse analysis.

The first inverse analysis model was developed by Barrick [13]. Only one sideband is used in the analysis and the water is assumed to be deep. Both sides of the equation are divided by the energy inside the first-order spectrum to remove the path losses and gains, assuming that they are the same for the first- and second-order radar returns.

Lipa [14] reduced Barrick's second-order cross section to a linear equation by means of a stabilization technique using a Phillips spectrum [15]. This technique significantly improves the results obtained from Barrick's model. She also derived a method for obtaining the directional features of the ocean spectrum. This is essentially the method used here for the bistatic case.

A detailed theoretical analysis was presented by Lipa and Barrick [16]. For pulsed

narrow beam Doppler radar systems the stabilization technique referred above was applied to the inverse analysis. A frequency band approximation and Fourier representation of ocean wave directional spectrum were invoked to convert the integral equation to a matrix equation. Several mathematical results and techniques were presented for the first time and accompanied by FORTRAN computer programs. Simulated radar data were used to examine the algorithm.

Lipa and Barrick's work [16] was extended by Wyatt [17] and Wyatt *et al.* [18] to derive ocean wave information from a greater range of Doppler frequencies. Subsequently, Lipa and Barrick [19] presented another extension to include an ocean region of arbitrary depth.

Howell [20] produced an algorithm for the inverse analysis by means of the singular value decomposition (SVD). Similar to Lipa and Barrick [16], the narrow beam monostatic second-order cross section was normalized by the energy inside the first-order peak to remove the path gains and losses. The resulting integral expression was linearized using a Phillip's equilibrium spectrum [15] and discretized using frequency bands. The directional ocean wave spectrum was represented by a truncated Fourier series. The matrix equation was then formed and the kernel matrix was pseudo-inverted by the SVD method.

In Howell's work [20], the algorithms for single radar and dual radar were developed. Three cross section models of Walsh *et al.* [10], Barrick and Lipa [7], and Srivastava [9] were checked and the results were compared with *in situ* measurements obtained from a WAVEC directional wave buoy. According to his analysis, the cross section model in [10] for dual-radar gives better agreement than either Barrick and Lipa's or Srivastava's. Howell demonstrated that for the narrow beam radar, the agreement between the magnitude of the recovered ocean wave non-directional spectrum from HF radar data and that of the buoy data was dependent, in some cases, on wind direction. The best agreement in magnitude occurred when the wind direction was parallel to the radar beam.

The worst result was obtained when the wind direction and radar beam direction are mutually perpendicular.

Howell [20] discussed the condition of stability for the inversion of kernel matrix. He found that the choice of the number  $r$  of singular values retained for the inversion is independent of sea state or wave direction. This  $r$ , an integer, is equal to or less than the rank of the kernel matrix.

Contemporary with Howell, Gill [21] achieved an algorithm to invert the wide beam HF radar monostatic cross section. A four-element square radar array, known as CODAR (Coastal Oceans Dynamics Applications Radar), was used to measure the wind-driven waves in a region where water depth was set to be arbitrary. The first- and second-order wide beam radar cross sections obtained by Barrick and Lipa [22] were applied to the four-element CODAR. The radar beam pattern and ocean wave spectrum were represented by Fourier coefficients. The wide beam second-order cross section was converted to a matrix equation after linearization and discretization procedures. The SVD method was invoked to pseudo-invert the kernel matrix and ocean wave directional wave spectra were obtained.

Gill [21] indicated that the number of singular values retained for inversion should be chosen from the region where the plot of the logarithm of the singular values against singular value position shows a steep change in slope. He also found, numerically, that the arrangement of kernel matrix would significantly affect the stability of the SVD. The better way to form the kernel matrix was letting rows associated with the increasingly large values of  $|\eta| - 1$  be adjacent to each other, where  $\eta$  is the Doppler frequency normalized by the wavenumber of the first-order peak. Gill's simulated results showed excellent agreement with original ocean wave non-directional models. Gill and Walsh [23] also presented results ground truthed by Wave Rider buoy data in which significant waveheight compared very favourably.

With the bistatic first- and second-order cross sections and a model of the noisy Doppler power spectral density now available, the inverse problem of extracting ocean surface parameters from simulated and real bistatic data may be considered.

### 1.3 Scope of the Thesis

An algorithm for the inverse problem for the bistatic scattering of HF radiation from the ocean surface is presented in this thesis. The radar is assumed to be operating in the upper level of the HF band (20 to 30 MHz). The transmit signal is vertically polarized and grazing incidence to the slightly rough ocean surface is assumed. The wind-driven ocean waves scatter the radar waves and a narrow beam radar receiver distant from the transmitter receives the echo. The water depth is set to be arbitrary. The limiting noise is assumed to be external to the system and to be zero-mean stationary Gaussian in nature.

Of the three components of the second-order bistatic cross section developed by Gill and Walsh [11], only the patch scatter is used because it is dominant when comparing with the other two parts. The first-order cross section is calculated in order to derive a normalizing factor for the entire spectrum. Normalization removes path gains and losses. The Newton-Raphson method is invoked to solve a delta function constraint appearing in the normalized cross section. This delta function enables the double integral in the second-order cross section to be reduced to a single integral.

The directional ocean wave spectrum is presented as the product of a non-directional wave spectrum and a directional distribution factor. The non-directional ocean wave spectrum is, according to Gill [12], one-half of the Pierson-Moskowitz spectrum [24]. The integral equation is linearized by means of the assumption that one of the two scattering waves responsible for second-order phenomena is in the saturated region of the ocean wave spectrum along with the Bragg wave. A truncated Fourier series is used

to represent the unknown ocean wave spectrum. Using a frequency band approximation and a discretization scheme, the integral equation is converted to a matrix equation. The SVD method is used to pseudo-invert the kernel matrix and the matrix equation is solved to obtain the non-directional ocean wave spectrum. The results of the inverse analysis are shown for different wind directions, wind speeds and water depths.

Chapter two contains the calculation of the bistatic first- and second-order cross sections. Chapter three describes the inverse problem analysis in detail and presents simulated results. Chapter four is concerned with the inverse problem when noise is added to the radar spectrum. Chapter five contains conclusions and suggestions for future work. Appendix A contains the *Matlab* computer programs associated with the inverse algorithm.

## Chapter 2

# Calculation of the Bistatic Cross Sections

### 2.1 General

HF Doppler radar spectra almost invariably consist of two well-defined peaks surrounded by a higher order continuum. As noted in Chapter 1, the underlying physical mechanism which accounts for this phenomenon was first conjectured by Crombie [2] to be Bragg scattering. The Doppler positions of the two peaks, denoted as the first-order or Bragg peaks, are symmetrical about the radar carrier frequency if surface currents are absent and are proportional to the square root of the radar operating wavenumber  $k_0$ .

The ocean surface layer is a dispersive medium for wind-driven gravity waves, and the phase speeds of these waves are proportional to their wavelengths. The relationship between the radian frequency,  $\omega$ , of an ocean wave, and the corresponding wavenumber  $K$  is ( see, for example, Kinsmen [25])

$$\omega = \sqrt{gK \tanh(dK)}, \quad (2.1)$$

where  $g$  is the acceleration due to gravity and  $d$  is water depth. Equation (2.1) is denoted as the linear dispersion relationship for water waves.

The position of the Bragg peaks in the Doppler spectrum (see Figure 1.1) matches the velocities of ocean waves whose wavelengths are equal to one-half the radar operating wavelength if grazing incidence and monostatic operation are assumed. Thus, for water waves traveling toward and away from the radar, the Doppler frequencies of the first-order peaks will occur at  $\pm\omega_B$ , respectively, where

$$\omega_B = \sqrt{2gk_0 \tanh(2dk_0)}. \quad (2.2)$$

For deep water, in which the water depth is greater than approximately one-half of the ocean wavelength, the hyperbolic tangent approaches unity, and the dispersion relationship in equation (2.1) simplifies to

$$\omega = \sqrt{gK}, \quad (2.3)$$

while the Doppler frequencies of the first-order peaks become from (2.2)

$$\omega_B = \pm\sqrt{2gk_0}. \quad (2.4)$$

To give background to the ensuing analysis, much of the remainder of this section summary is extracted from the relevant portions of the bistatic analyses developed by Gill and Walsh [11].

The geometry of the bistatic configuration is depicted in Figure 2.1. The path directed from the transmitter (T) to the receiver (R) is the reference line. T and R are foci of an elliptical scattering patch. P is a position on this ellipse where the unit normal is

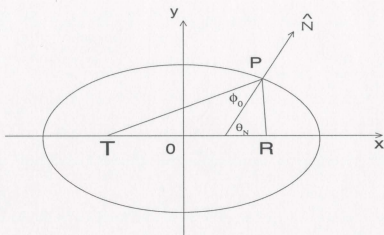


Figure 2.1: The geometrical relationship of the bistatic configuration.

$\hat{N}$ . The angle  $\theta_N$  from  $\overline{TR}$  to the unit normal is precisely the direction of the scattering wavevector in the first-order cross section. The angle  $\angle TPR$  is bisected by the ellipse normal. Half of  $\angle TPR$  is defined as the bistatic angle  $\phi_0$ .

For bistatic scattering, the Doppler frequencies of the first-order peaks are a function of  $\phi_0$  as given by

$$\omega_B = \pm \sqrt{2gk_0 \cos \phi_0 \tanh(2dk_0 \cos \phi_0)}. \quad (2.5)$$

For deep water

$$\omega_B = \pm \sqrt{2gk_0 \cos \phi_0}. \quad (2.6)$$

The bistatic first-order and second-order cross sections developed by Gill and Walsh [11] are reproduced here and calculated in the following sections. Only the first- and second-order cross sections of patch scattering are considered for the inverse analysis.

The first-order cross section  $\sigma_1(\omega)$  is given as [11]

$$\sigma_1(\omega) = 2^4 \pi k_0^2 \sum_{m=\pm 1} S_1(m\vec{K}) \frac{K^{\frac{5}{2}} \cos \phi_0}{\sqrt{g}} \Delta \rho_s S a^2 \left[ \frac{\Delta \rho_s}{2} \left( \frac{K}{\cos \phi_0} - 2k_0 \right) \right]. \quad (2.7)$$

Here  $\omega$  is the radian Doppler frequency and  $S_1(m\vec{K})$  is the directional wave spectrum with the scattering wave vector  $\vec{K}$ .  $\Delta \rho_s$  is the scattering patch width illuminated by a radar pulse. It is the smallest radial distance that can be unambiguously distinguished by the radar and is given by

$$\Delta \rho_s = \frac{c\tau_0}{2}, \quad (2.8)$$

where  $c$  is the light speed and  $\tau_0$  is the pulse width of the transmitted signal;  $m = \pm 1$  indicates the various positive and negative portions of the of Doppler shift corresponding to the ocean waves moving toward and backward to the direction of ellipse normal (see Figure 2.2). i.e.

$$m = 1 \text{ when } \omega < 0 \quad (2.9)$$

and

$$m = -1 \text{ when } \omega > 0. \quad (2.10)$$

The Doppler frequency is related to the scattering wave number  $K$  by the dispersion relationship as

$$\omega = -m\sqrt{gK}. \quad (2.11)$$

It may be noted that instead of the delta function appearing in Barrick's first-order cross

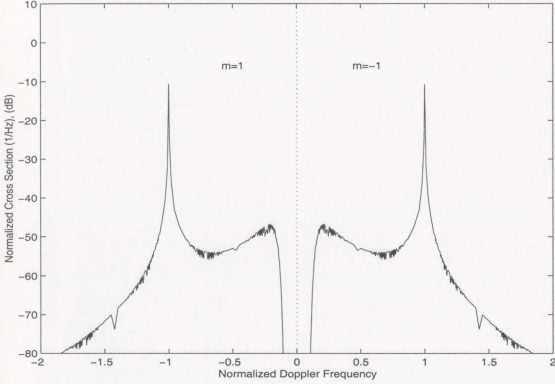


Figure 2.2: The two sections of the bistatic first-order cross section.

section expression [4], a squared sampling function generates the first-order peaks here.

The second-order cross section for patch scattering is given by

$$\sigma_{2P}(\omega) \approx 2^6 \pi^2 k_0^4 \cos^4 \phi_0 \sum_{m_1=\pm 1} \sum_{m_2=\pm 1} \int_{-\pi}^{\pi} \int_0^{\infty} S_1(m_1 \vec{K}_1) S_1(m_2 \vec{K}_2) \cdot |S\Gamma_P|^2 \delta\left(\omega + m_1 \sqrt{gK_1} + m_2 \sqrt{gK_2}\right) K_1 dK_1 d\theta_{\vec{K}_1}, \quad (2.12)$$

where  $\delta(\cdot)$  is a delta function and the remaining parameters are defined in the following paragraphs.  $\vec{K}_1$  and  $\vec{K}_2$  are the wave vectors of the ocean waves responsible for first and second scatters, respectively, upon the surface. In order for the second-order bistatic scattering to occur,  $\vec{K}_1$  and  $\vec{K}_2$  must obey the condition,

$$\vec{K}_1 + \vec{K}_2 = \vec{K} \quad (2.13)$$

as shown in Figure 2.3. Here  $\vec{K}$  has the direction  $\theta_N$  of the ellipse normal (see Figure 2.1)

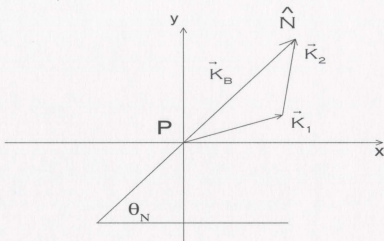


Figure 2.3: An enlarged view of the second-order scattering wave vectors for the bistatic patch scatterer.

and a magnitude of  $2k_0 \cos \phi_0$ . Using the law of cosines (see Figure 2.3), the magnitude of  $\vec{K}_2$  may be obtained from

$$\begin{aligned}
 K_2^2 &= K_1^2 + K^2 - 2K_1K \cos(\theta_{\vec{K}_1} - \theta_N) \\
 &= K_1^2 + 4k_0^2 \cos^2 \phi_0 - 4K_1k_0 \cos \phi_0 \cos(\theta_{\vec{K}_1} - \theta_N) .
 \end{aligned} \tag{2.14}$$

where  $\theta_{\vec{K}_1}$  is the angle of  $\vec{K}_1$  from the  $x$ -axis.

The four possible combinations of  $m_1$  and  $m_2$  represent four different Doppler frequency regions, corresponding to four sidebands of second-order cross section (see Figure 2.4). These four parts are denoted as  $P_1$ ,  $P_2$ ,  $P_3$ , and  $P_4$  from left to right, respectively.

If  $m_1 = m_2$ ,

$$\left. \begin{aligned}
 \omega < -\omega_B, & \text{ when } m_1 = m_2 = 1 \\
 \omega > \omega_B, & \text{ when } m_1 = m_2 = -1
 \end{aligned} \right\} . \tag{2.15}$$

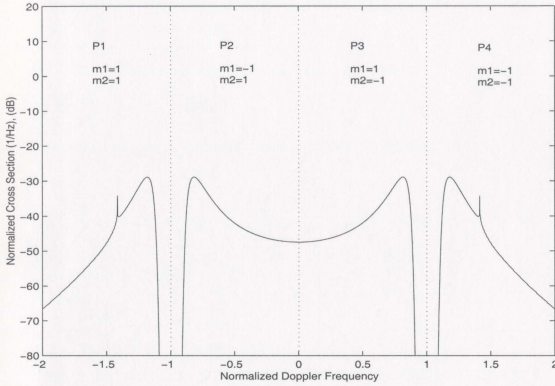


Figure 2.4: The four sections of the bistatic second-order cross section. Only  $K_1 < K_2$  case is denoted here.

If  $m_1 \neq m_2$ ,  $-\omega_B < \omega < \omega_B$ , and

$$\left. \begin{array}{l}
 -\omega_B < \omega < 0, \quad \left. \begin{array}{l} m_1 = -1, m_2 = +1 \text{ if } K_1 < K_2 \text{ or} \\ m_1 = +1, m_2 = -1 \text{ if } K_1 > K_2 \end{array} \right\} \\
 \text{and} \\
 0 < \omega < \omega_B, \quad \left. \begin{array}{l} m_1 = -1, m_2 = +1 \text{ if } K_1 > K_2 \text{ or} \\ m_1 = +1, m_2 = -1 \text{ if } K_1 < K_2 \end{array} \right\}
 \end{array} \right\} . \quad (2.16)$$

It is observed that the second-order cross section possesses a symmetry around the Bragg frequencies  $\pm\omega_B$ . This property will help to reduce the complexity of the ensuing calculation. In the inverse analysis, only the  $K_1 < K_2$  case need to be considered.

In equation (2.12), the symmetric coupling coefficient  $s\Gamma_P$  is defined as

$$s\Gamma_P = \frac{1}{2} \left[ \Gamma_P(\vec{K}_1, \vec{K}_2) + \Gamma_P(\vec{K}_2, \vec{K}_1) \right], \quad (2.17)$$

here

$$\Gamma_P = {}_H\Gamma_P + {}_E\Gamma_P. \quad (2.18)$$

The hydrodynamic coupling coefficient,  ${}_H\Gamma_P$  is given by Walsh *et al.* [10]. For water of arbitrary depth,

$${}_H\Gamma_P = \frac{-g^2}{\omega_1\omega_2} \left\{ \frac{j(\omega_1 + \omega_2)}{g[gK \tanh(Kd) - (\omega_1 + \omega_2)^2]} D_{\vec{K}_1, \vec{K}_2}^{\omega_1, \omega_2} + E_{\vec{K}_1, \vec{K}_2}^{\omega_1, \omega_2} \right\}, \quad (2.19)$$

where

$$\begin{aligned} D_{\vec{K}_1, \vec{K}_2}^{\omega_1, \omega_2} &= j(\omega_1 + \omega_2) [K_1 K_2 \tanh(K_1 d) \tanh(K_2 d) - \vec{K}_1 \cdot \vec{K}_2] \\ &\quad - \frac{j}{2} \left[ \frac{\omega_1 K_2^2}{\cosh^2(K_2 d)} + \frac{\omega_2 K_1^2}{\cosh^2(K_1 d)} \right] \end{aligned} \quad (2.20)$$

and

$$E_{\vec{K}_1, \vec{K}_2}^{\omega_1, \omega_2} = \frac{1}{2g} \left\{ (\vec{K}_1 \cdot \vec{K}_2) - g^{-2} \omega_1 \omega_2 (\omega_1^2 + \omega_2^2 + \omega_1 \omega_2) \right\}. \quad (2.21)$$

Here  $\omega_1$  and  $\omega_2$  are the radian frequencies of the ocean waves involved in the scattering process. For deep water, the hydrodynamic coupling coefficient is simplified as

$${}_H\Gamma_P = \frac{1}{2} \left\{ K_1 + K_2 + \frac{g}{\omega_1 \omega_2} (K_1 K_2 - \vec{K}_1 \cdot \vec{K}_2) \left[ \frac{gK + (\omega_1 + \omega_2)^2}{gK - (\omega_1 + \omega_2)^2} \right] \right\}, \quad (2.22)$$

where  $K = 2k_0 \cos \phi_0$ ,  $\omega_1 = -m_1 \sqrt{gK_1}$ , and  $\omega_2 = -m_2 \sqrt{gK_2}$ .

The electromagnetic coupling coefficient,  ${}_E\Gamma_P$  is given as [12]

$${}_E\Gamma_P(\vec{K}_1, \vec{K}_2) = \left\{ \frac{j\sqrt{\vec{K}_1 \cdot (\vec{K}_1 - 2k_0\hat{\rho}_2)} + k_0}{k_0^2 + \vec{K}_1 \cdot (\vec{K}_1 - 2k_0\hat{\rho}_2)} \right\}$$

$$\left\{ \frac{(\vec{K}_1 \cdot \hat{\rho}_2) [\vec{K}_2 \cdot (\vec{K}_1 - k_0 \hat{\rho}_2)]}{\sqrt{\vec{K}_1 \cdot (\vec{K}_1 - 2k_0 \hat{\rho}_2)}} \right\}, \quad (2.23)$$

where  $j = \sqrt{-1}$  and  $\hat{\rho}_2$  is the normalized vector along the receiving path ( $\overline{PR}$  on Figure 2.1). The other part,  ${}_E\Gamma_P(\vec{K}_2, \vec{K}_1)$  may be obtained by interchanging the  $\vec{K}_1$  and  $\vec{K}_2$ .

The hydrodynamic and electromagnetic coupling coefficients correspond to two mechanisms for the second-order interactions between the radar signal and water waves. From Hasselmann's theory [26], the so-called hydrodynamic term arises due to the signal interacting with a second-order ocean wave formed from two interacting waves whose wavenumbers are satisfied by  $\vec{K}_1 + \vec{K}_2 = \vec{K}$ . On the other hand, the electromagnetic term involves two first-order scatterings. This means that the incident radar wave is scattered by a first-order ocean wave of wavenumber  $K_1$ , and this scattered signal is scattered again by another first-order ocean wave of wavenumber  $K_2$ . These two first-order scatters occur on the scattering patch. If the scattering wave vectors satisfy equation (2.13), the scattered energy will appear in the radar spectrum. Since there are many combinations of  $\vec{K}_1$  and  $\vec{K}_2$  that satisfy the second-order scattering condition, the inversion of the second-order cross section may lead to the extraction of ocean wave information for a significant range of wavenumbers.

In the following sections, the first- and second-order cross sections are calculated. The calculation of the first-order cross section involves an expression for the angular frequency of the Bragg peaks, which will be used as the normalizing factor for the second-order cross section. The energy inside the first-order peaks is derived so that it may be used to normalize the overall spectrum and calculate the wind direction, approximately. Once the second-order cross section is normalized, the dual-integral of equation (2.12) will be reduced to a single integral via the numerical solution of the delta function.

## 2.2 Calculation of the First-order Cross Section

For the purpose of determining the Bragg wave scattering vector the squared sampling function in the first-order cross section can be approximated under the assumption that the scattering patch width,  $\Delta\rho_s$ , is large. Since

$$\lim_{M \rightarrow \infty} MSa^2 [Mx] = \pi\delta(x) , \quad (2.24)$$

we have

$$\begin{aligned} & \lim_{\frac{\Delta\rho_s}{2 \cos \phi_0} \rightarrow \infty} Sa^2 \left[ \frac{\Delta\rho_s}{2 \cos \phi_0} (K - 2k_0 \cos \phi_0) \right] \\ = & \frac{2 \cos \phi_0}{\Delta\rho_s} \lim_{\frac{\Delta\rho_s}{2 \cos \phi_0} \rightarrow \infty} \frac{\Delta\rho_s}{2 \cos \phi_0} Sa^2 \left[ \frac{\Delta\rho_s}{2 \cos \phi_0} (K - 2k_0 \cos \phi_0) \right] \\ \approx & \frac{2\pi \cos \phi_0}{\Delta\rho_s} \delta(K - 2k_0 \cos \phi_0) . \end{aligned} \quad (2.25)$$

This means that equation (2.7) can be approximated as

$$\sigma_1(\omega) = \frac{2^5 \pi^2 k_0^2 \cos^2 \phi_0}{\sqrt{g}} \sum_{m=\pm 1} S_1(m\vec{K}) K^{\frac{5}{2}} \delta(K - 2k_0 \cos \phi_0) . \quad (2.26)$$

Imposing the delta function constraint, we can see that the first-order maximum will occur when

$$K = K_B = 2k_0 \cos \phi_0 . \quad (2.27)$$

This is the wavenumber  $K_B$  associated with the Bragg peaks for bistatic scattering. It is clearly a function of bistatic angle  $\phi_0$ . When  $\phi_0 = 0$ , we have the wavenumber  $K_{B_{mono}}$

associated with the Bragg peaks for monostatic scattering, namely

$$K_{B_{mono}} = 2k_0 . \quad (2.28)$$

In order that the analysis may be readily used for any operating frequency of interest, it is convenient to normalize the wavenumbers and Doppler frequencies by their Bragg counterparts (see, for example [23] or [27]). In the case of wavenumbers, the normalizing factor is thus  $K_B = 2k_0 \cos \phi_0$ . Then, the normalized wave vector is

$$\vec{K}_n = \frac{\vec{K}}{2k_0 \cos \phi_0} \quad (2.29)$$

and the normalized wavenumber is

$$K_n = \frac{K}{2k_0 \cos \phi_0} . \quad (2.30)$$

For consistency, the other dimensionless quantities of normalization are obtained as follows: Normalized water depth  $D$ :

$$D = d \cdot 2k_0 \cos \phi_0 . \quad (2.31)$$

Normalized Doppler frequency  $\eta$ :

$$\begin{aligned} \eta = \frac{\omega}{\omega_B} &= \frac{\sqrt{gK \tanh(Kd)}}{\sqrt{2gk_0 \cos \phi_0 \tanh(2dk_0 \cos \phi_0)}} \\ &= \frac{\sqrt{K_n \tanh(K_n D)}}{\sqrt{\tanh D}} . \end{aligned} \quad (2.32)$$

Normalized ocean wave spectrum  $Z(\cdot)$ :

$$Z_1(m\vec{K}_n) = (2k_0 \cos \phi_0)^4 S_1(m\vec{K}) . \quad (2.33)$$

Then, the first-order cross section in normalized form is given as

$$\sigma_{1n}(\eta) = \omega_B \sigma_1(\omega) = 2^3 \pi k_0 \sum_{m=\pm 1} Z_1(m\vec{K}_n) K_n^{\frac{5}{2}} \Delta \rho_s S a^2 [\Delta \rho_s k_0 (K_n - 1)] . \quad (2.34)$$

As noted, the energy inside the first-order cross section,  $E_{m1}$ , can be used to linearize the second-order cross section in the inverse problem. The purpose of doing this is to remove the signal path gains and losses affecting the radar spectrum. The assumption is that the gains and losses associated with the first-order case are the same as those in the second-order case. The normalized first-order cross section may be integrated over the radian frequency to give

$$E_{m1} = \int_{\eta} \sigma_{1n}(\eta) d\eta . \quad (2.35)$$

The differential of the normalized radian frequency may be converted to the differential of the normalized wavenumber. That is, from equation (2.32)

$$d\eta = \frac{\tanh(K_n D) + K_n D \operatorname{sech}^2(K_n D)}{2\sqrt{\tanh D} \sqrt{K_n \tanh(K_n D)}} dK_n = T_n dK_n . \quad (2.36)$$

Then equation (2.35) becomes

$$E_{m1} = \int_{-\infty}^{\infty} 2^3 \pi k_0 \sum_{m=\pm 1} Z_1(m\vec{K}_n) K_n^{\frac{5}{2}} \Delta \rho_s S a^2 [\Delta \rho_s k_0 (K_n - 1)] T_n dK_n . \quad (2.37)$$

When the scattering patch is large, the squared sampling function can be approximated

as a delta function. According to equation (2.24), equation (2.37) becomes

$$\begin{aligned}
 E_{m1} &= \int_{-\infty}^{\infty} 2^3 \pi^2 \sum_{m=\pm 1} Z_1(m\vec{K}_n) K_n^{\frac{5}{2}} \delta(K_n - 1) T_n dK_n \\
 &= 2^2 \pi^2 \left[ 1 + \frac{D \operatorname{sech}^2(D)}{\tanh D} \right] \sum_{m=\pm 1} Z_1(m \cdot 1), \tag{2.38}
 \end{aligned}$$

where  $Z_1(m \cdot 1)$  is normalized ocean wave directional spectrum with the normalized wavenumber  $K_n = 1$  (i.e. the normalized Bragg wavenumber).

Practically, the total energy inside the first-order cross section cannot be obtained precisely because of the infinite integral limits. However, this energy can be approximated in a finite range,  $\pm k_c$  around the first-order peaks, since most of the energy is concentrated in this range. (See *Matlab* subroutine *FirstOrder.m* in Appendix A)

## 2.3 Calculation of the Second-order Cross Section

### 2.3.1 Normalized Version of Second-order Cross Section

As was done for the first-order cross section, the normalized form of the second-order cross section of patch scattering is calculated from equation (2.12). The first step is to define dimensionless variables for the second-order cross section. In addition to those appearing in equations (2.29) to (2.33), we define the normalized coupling coefficients as

$$\Gamma_n = \frac{\Gamma}{2k_0 \cos \phi_0} \tag{2.39}$$

and normalized second-order cross section as

$$\sigma_{2n}(\eta) = \omega_B \sigma(\omega) . \tag{2.40}$$

Then, for water of arbitrary depth, the normalized version of the second-order cross section is

$$\sigma_{2pn}(\eta) = 2^2 \pi^2 \sum_{m_1=\pm 1} \sum_{m_2=\pm 1} \int_{-\pi}^{\pi} \int_0^{\infty} Z_1(m_1 \vec{K}_{1n}) Z_1(m_2 \vec{K}_{2n}) |{}_S \Gamma_{pn}|^2 \delta \left[ \eta + \frac{m_1 \sqrt{K_{1n} \tanh(K_{1n} D)}}{\sqrt{\tanh(D)}} + \frac{m_2 \sqrt{K_{2n} \tanh(K_{2n} D)}}{\sqrt{\tanh(D)}} \right] K_{1n} dK_{1n} d\theta_{\vec{K}_{1n}}. \quad (2.41)$$

The normalized version of the hydrodynamic coupling coefficient for shallow water,  ${}_H \Gamma_{pn}$ , derived from equation (2.19) to (2.21), is

$${}_H \Gamma_{pn} = \frac{1}{\eta_1 \eta_2 \tanh D} \left\{ \frac{(\eta_1 + \eta_2)}{[1 - (\eta_1 + \eta_2)^2]} D_{\vec{K}_{1n}, \vec{K}_{2n}}^{\eta_1, \eta_2} - E_{\vec{K}_{1n}, \vec{K}_{2n}}^{\eta_1, \eta_2} \right\}, \quad (2.42)$$

where

$$D_{\vec{K}_{1n}, \vec{K}_{2n}}^{\eta_1, \eta_2} = (\eta_1 + \eta_2) [K_{1n} K_{2n} \tanh(K_{1n} D) \tanh(K_{2n} D) - \vec{K}_{1n} \cdot \vec{K}_{2n}] - \frac{1}{2} \left[ \frac{\eta_1 K_{2n}^2}{\cosh^2(K_{2n} D)} + \frac{\eta_2 K_{1n}^2}{\cosh^2(K_{1n} D)} \right] \quad (2.43)$$

and

$$E_{\vec{K}_{1n}, \vec{K}_{2n}}^{\eta_1, \eta_2} = \frac{1}{2} \left[ (\vec{K}_{1n} \cdot \vec{K}_{2n}) - \eta_1 \eta_2 (\eta_1^2 + \eta_2^2 + \eta_1 \eta_2) \tanh^2 D \right]. \quad (2.44)$$

The normalized version of the electromagnetic coupling coefficient is

$$E \Gamma_{Pn}(\vec{K}_{1n}, \vec{K}_{2n}) = \left\{ \frac{j \sqrt{\vec{K}_{1n} \cdot \left( \vec{K}_{1n} - \frac{\hat{\rho}_2}{\cos \phi_0} \right)} + \frac{1}{2 \cos \phi_0}}{\frac{1}{(2 \cos \phi_0)^2} + \vec{K}_{1n} \cdot \left( \vec{K}_{1n} - \frac{\hat{\rho}_2}{\cos \phi_0} \right)} \right\}$$

$$\left\{ \frac{(\vec{K}_{1n} \cdot \hat{\rho}_2) \left[ \vec{K}_{2n} \cdot \left( \vec{K}_{1n} - \frac{\hat{\rho}_2}{2 \cos \phi_0} \right) \right]}{\sqrt{\vec{K}_{1n} \cdot \left( \vec{K}_{1n} - \frac{\hat{\rho}_2}{\cos \phi_0} \right)}} \right\} . \quad (2.45)$$

The constraint on the normalized scattering wavenumbers so that the second-order scattering will occur is

$$\vec{K}_{1n} + \vec{K}_{2n} = \vec{K}_n , \quad (2.46)$$

where  $\vec{K}_n$  has the direction of the scattering ellipse normal and a magnitude of unity.

From the law of cosines,  $K_{2n}$  is expressed in terms of  $K_{1n}$  as

$$K_{2n}^2 = K_{1n}^2 + 1 - 2K_{1n} \cos(\theta_{\vec{K}_{1n}} - \theta_N) . \quad (2.47)$$

In reworking equation (2.41) for the calculation of  $\sigma_{2pn}(\eta)$ , consider defining

$$Y_n = \sqrt{K_{1n}} . \quad (2.48)$$

Then,

$$K_{1n} dK_{1n} = 2Y_n^3 dY_n . \quad (2.49)$$

The delta function constraint may now be rewritten as

$$\delta(\cdot) = \delta \left[ \eta - D_P(Y_n, \theta_{\vec{K}_1}) \right] , \quad (2.50)$$

where

$$D_P(Y_n, \theta_{\vec{K}_1}) = \frac{-m_1 \sqrt{K_{1n} \tanh(K_{1n} D)} - m_2 \sqrt{K_{2n} \tanh(K_{2n} D)}}{\sqrt{\tanh(D)}}$$

$$\begin{aligned}
&= \frac{-m_1 Y_n \sqrt{\tanh(Y_n^2 D)}}{\sqrt{\tanh(D)}} - \frac{m_2}{\sqrt{\tanh(D)}} \\
&\cdot \left[ Y_n^4 + 1 - 2Y_n^2 \cos(\theta_{\bar{K}_{1n}} - \theta_N) \right]^{\frac{1}{4}} \\
&\cdot \sqrt{\tanh \left[ \left( Y_n^4 + 1 - 2Y_n^2 \cos(\theta_{\bar{K}_{1n}} - \theta_N) \right)^{\frac{1}{2}} D \right]}. \quad (2.51)
\end{aligned}$$

Since

$$dY_n = \left| \frac{\partial Y_n}{\partial D_p} \right| dD_p = J_{tn} dD_p, \quad (2.52)$$

where  $J_{tn} = \left| \frac{\partial Y_n}{\partial D_p} \right|$  is denoted as the normalized Jacobian of the transformation,

$$K_{1n} dK_{1n} = 2Y_n^3 J_{tn} dD_p. \quad (2.53)$$

Now equation (2.41) may be rewritten as

$$\begin{aligned}
\sigma_{2pn}(\eta) &= 2^3 \pi^2 \sum_{m_1=\pm 1} \sum_{m_2=\pm 1} \int_{-\pi}^{\pi} \int_0^{\infty} Z_1(m_1 \bar{K}_{1n}) Z_1(m_2 \bar{K}_{2n}) |S\Gamma_{pn}|^2 \\
&\delta[\eta - D_P(Y_n, \theta_{\bar{K}_1})] J_{tn} Y_n^3 dD_p d\theta_{\bar{K}_{1n}}. \quad (2.54)
\end{aligned}$$

The expression for  $J_{tn}$  is

$$J_{tn} = \frac{\sqrt{\tanh(D)}}{|J_D|}. \quad (2.55)$$

Here

$$\begin{aligned}
J_D &= m_1 \frac{\tanh(Y_n^2 D) + Y_n^2 D \operatorname{sech}^2(Y_n^2 D)}{\sqrt{\tanh(Y_n^2 D)}} + m_2 \frac{Y_n^3 - Y_n \cos(\theta_{\bar{K}_{1n}} - \theta_N)}{K_{2n}^{\frac{3}{2}}} \\
&\cdot \frac{\tanh(K_{2n} D) + K_{2n} D \operatorname{sech}^2(K_{2n} D)}{\sqrt{\tanh(K_{2n} D)}}, \quad (2.56)
\end{aligned}$$

where  $K_{2n}$  is expressed as equation (2.47) with  $K_{1n}$  replaced by  $Y_n^2$ . When the water is deep, we have  $\tanh(D) \approx 1$  and  $\operatorname{sech}(K_{2n}D) \approx 0$ . In this case,  $J_{tn}$  reduces to

$$J_{tnd} = \frac{1}{m_1 + m_2 \frac{Y_n^3 - Y_n \cos(\theta_{\vec{K}_{1n}} - \theta_N)}{[Y_n^4 + 1 - 2Y_n \cos(\theta_{\vec{K}_{1n}} - \theta_N)]^{3/4}}}. \quad (2.57)$$

### 2.3.2 The Solution of the Delta Function Constraint

The dual-integral equation in the second-order cross section is reduced to a single integral equation by means of the solution of delta function constraint. This means solving

$$\eta - D_P(Y_n, \theta_{\vec{K}_1}) = 0. \quad (2.58)$$

Suppose that the value  $Y_n^*$  is solution of the delta function constraint. We can use  $Y_n^*$  to replace  $Y_n$  in the previous equation. Equation (2.54) is simplified as

$$\sigma_{2pn}(\eta) = 2^3 \pi^2 \sum_{m_1=\pm 1} \sum_{m_2=\pm 1} \int_{-\pi}^{\pi} Z_1(m_1 \vec{K}_{1n}) Z_1(m_2 \vec{K}_{2n}) |S \Gamma_{pn}|^2 J_{tn} Y_n^2 |_{Y_n=Y_n^*} d\theta_{\vec{K}_{1n}}. \quad (2.59)$$

The Newton-Raphson method is invoked here to derive the wavenumber  $K_{1n}$  for each wave frequency  $\eta$  and scattering angle  $\theta_{\vec{K}_1}$ . The spirit of the method is to numerically solve a function

$$G(Y_n) = \eta - D_P(Y_n, \theta_{\vec{K}_1}). \quad (2.60)$$

Of course,

$$G(Y_n^*) = 0. \quad (2.61)$$

Next,  $G(Y_n)$  is expanded about  $Y_n^*$  by means of the Taylor series.

$$\begin{aligned} G(Y_n) &\approx G(Y_n^*) + (Y_n - Y_n^*) \left( \frac{\partial G(Y_n)}{\partial Y_n} \right)_{Y_n=Y_n^*} \\ &\approx (Y_n - Y_n^*) \left( \frac{\partial G(Y_n)}{\partial Y_n} \right)_{Y_n=Y_n^*}, \end{aligned} \quad (2.62)$$

i.e.

$$Y_n^* \approx Y_n - \frac{G(Y_n)}{\left( \frac{\partial G}{\partial Y_n} \right)_{Y_n=Y_n^*}}. \quad (2.63)$$

From the relationship between  $K_{1n}$  and  $K_{2n}$  (equation(2.47)),  $G(Y_n)$  can be written as

$$\begin{aligned} G(Y_n) &= \eta - D_P \left( Y_n, \theta_{\bar{K}_1} \right) \\ &= \eta + \frac{m_1 \sqrt{K_{1n} \tanh(K_{1n} D)} + m_2 \sqrt{K_{2n} \tanh(K_{2n} D)}}{\sqrt{\tanh(D)}} \\ &= \eta + \frac{m_1 Y_n \sqrt{\tanh(Y_n^2 D)}}{\sqrt{\tanh(D)}} + \frac{m_2 (Y_n^4 + 1 - 2Y_n^2 \cos(\theta_{\bar{K}_{1n}} - \theta_N))^{1/4}}{\sqrt{\tanh(D)}} \\ &\quad \cdot \sqrt{\tanh \left[ (Y_n^4 + 1 - 2Y_n^2 \cos(\theta_{\bar{K}_{1n}} - \theta_N))^{1/2} D \right]}. \end{aligned} \quad (2.64)$$

Then, the derivative of equation (2.64) gives

$$\begin{aligned} \frac{\partial G(Y_n)}{\partial Y_n} &= \frac{1}{\sqrt{\tanh(D)}} \left\{ m_1 \frac{\tanh(Y_n^2 D) + Y_n^2 D \operatorname{sech}^2(Y_n^2 D)}{\sqrt{\tanh(Y_n^2 D)}} \right. \\ &+ m_2 \frac{Y_n^3 - Y_n \cos(\theta_{\bar{K}_{1n}} - \theta_N)}{\left[ Y_n^4 + 1 - 2Y_n^2 \cos(\theta_{\bar{K}_{1n}} - \theta_N) \right]^{3/4}} \\ &\quad \cdot \left[ \sqrt{\tanh(Y_n^4 + 1 - 2Y_n^2 \cos(\theta_{\bar{K}_{1n}} - \theta_N))^{1/2} D} \right. \\ &\quad \left. \left. + (Y_n^4 + 1 - 2Y_n^2 \cos(\theta_{\bar{K}_{1n}} - \theta_N))^{1/2} \right] \right\} \end{aligned}$$

$$\left. \frac{D \operatorname{sech}^2 \left( Y_n^4 + 1 - 2Y_n^2 \cos \left( \theta_{\vec{K}_{1n}} - \theta_N \right) \right)^{\frac{1}{2}} D}{\sqrt{\tanh \left( Y_n^4 + 1 - 2Y_n^2 \cos \left( \theta_{\vec{K}_{1n}} - \theta_N \right) \right)^{\frac{1}{2}} D}} \right\} . \quad (2.65)$$

We now need an initial guess of  $Y_n^*$ , say  $Y_{n_i}^*$ , in equation (2.63) to find the next  $Y_n^*$ , denoted as  $Y_{n(i+1)}^*$ . The calculation of  $|Y_{n(i+1)}^* - Y_{n_i}^*|$  continues until  $|Y_{n(i+1)}^* - Y_{n_i}^*| < \epsilon$ , where  $\epsilon$  is a specified tolerance. In our calculation,  $\epsilon = 0.001$  is used. The last value of  $Y_n^*$  so calculated is chosen as the solution of the delta function.

The determination of a suitable initial guess, as discussed by Lipa and Barrick [16], is from equation (2.61). Close to the Bragg peaks,  $Y_{1n} \ll 1$ . With the assumption of deep water, which means  $\tanh(D) \approx 1$ , equation (2.61) gives

$$Y_n^* \approx m_1 (\eta - m_2) . \quad (2.66)$$

It has been shown numerically (see programs in Appendix A) that the initial guess of (2.66) is suitable for the calculation in all parts of the Doppler spectrum.

### 2.3.3 The Choice of a Directional Ocean Wave Spectrum

The choice of an ocean spectral model has been discussed by Gill [12]. Generally, ocean spectral models may be considered as a product of a non-directional spectrum,  $S_1(K)$ , and a normalized directional distribution,  $g(\theta_{\vec{K}})$ , i.e.

$$S_1(\vec{K}) = S_1(K)g(\theta_{\vec{K}}) , \quad (2.67)$$

where  $g(\theta_{\vec{K}})$  satisfies the relation as explained in [28]

$$\int_0^{2\pi} g(\theta_{\vec{K}}) d\theta_{\vec{K}} = 1 . \quad (2.68)$$

Obviously,

$$\int_0^{2\pi} S_1(\vec{K}) = \int_0^{2\pi} S_1(K)g(\theta_{\vec{R}})d\theta_{\vec{R}} = S_1(K). \quad (2.69)$$

Gill [12] defines  $S_1(K)$  by means of the Pierson-Moskowitz spectrum as

$$S_1(K) = \frac{1}{2}S_{PM}(K), \quad (2.70)$$

where

$$S_{PM}(K) = \frac{\alpha_{PM}}{2K^4} e^{-\frac{0.74g^2}{K^2u^4}}. \quad (2.71)$$

Here  $\alpha_{PM}$  is a constant with a value 0.0081 while  $u$  is the wind speed measured at 19.5 m above the ocean surface. As a result of (2.70), Gill's [12] cross section is 3 dB lower in the first-order and 6 dB lower in the second-order power spectral density than other investigators [6], [9], and[10].

In equation (2.67), the directional distribution  $g(\theta_{\vec{R}})$ , which is a function of frequency, can be expressed as

$$g(\theta_{\vec{R}}, K) = F(s(K)) \cos^{2(s(K))} \left[ \frac{\theta_{\vec{R}} - \bar{\theta}(K)}{2} \right], \quad (2.72)$$

where  $s(K)$  is the so-called spread function and  $\bar{\theta}(K)$  is the dominant direction of the waves [28]. In simulating the HF radar cross section,  $\bar{\theta}(K)$  is usually replaced by  $\bar{\theta}$ , which is the wind direction with respect to the radar beam direction. We can further remove the dependence of frequency from the spread function for practical purposes [28]. Then, the simplified directional distribution is

$$g(\theta_{\vec{R}}) = F(s) \cos^{2s} \left[ \frac{\theta_{\vec{R}} - \bar{\theta}}{2} \right]. \quad (2.73)$$

In order to satisfy the equation (2.68),  $F(s)$  is defined as

$$F(s) = \frac{2^{(2s-1)}\Gamma^2(s+1)}{\pi\Gamma(2s+1)}, \quad (2.74)$$

where  $\Gamma$  is the gamma function. When  $s$  is an integer value  $F(s)$  can be expressed as

$$F(s) = F(s-1) \frac{s}{s-0.5} \quad (2.75)$$

with  $F(1) = \frac{1}{\pi}$ . In our calculation of simulated radar cross sections, a value of  $s = 2$  is used for consistency with a previous investigation [12]. That is,

$$F(s=2) = \frac{4}{3\pi}. \quad (2.76)$$

Then the directional ocean wave spectrum is obtained as

$$S_1(m\vec{K}) = \left[ \frac{\alpha_{PM}}{4K^4} e^{\frac{-0.74g^2}{K^2v^4}} \right] \left[ \frac{4}{3\pi} \cos^4 \left( \frac{\theta_{\vec{K}} + \frac{(1-m)\pi}{2} - \theta_w}{2} \right) \right], \quad (2.77)$$

where  $\theta_w$  is the wind direction with respect to the reference direction. Throughout the thesis, the directional ocean wave model given by equation(2.77) is used.

There are singularities in the integrand of equation (2.59) which must be considered in the calculation of the bistatic cross section. The sources of the singularities are the Jacobian of the transformation of equation (2.56) and the electromagnetic coupling coefficient of equation (2.45).

As in Gill's analysis, for deep water [12], when  $\theta_{\vec{K}_{1n}} = \theta_N$ ,  $Y_n = \frac{1}{\sqrt{2}}$ , and  $m_1m_2 = 1$ , the denominator of the normalized Jacobian of the transformation vanishes. The positions of the singularities are at  $\eta = \pm\sqrt{2}$ . Figure 2.5 depicts the combination of first- and second-order cross sections. Two  $F_Bs$  denote the first-order peaks. The  $J_s$ 's are the singularities from the Jacobian of the transformation.

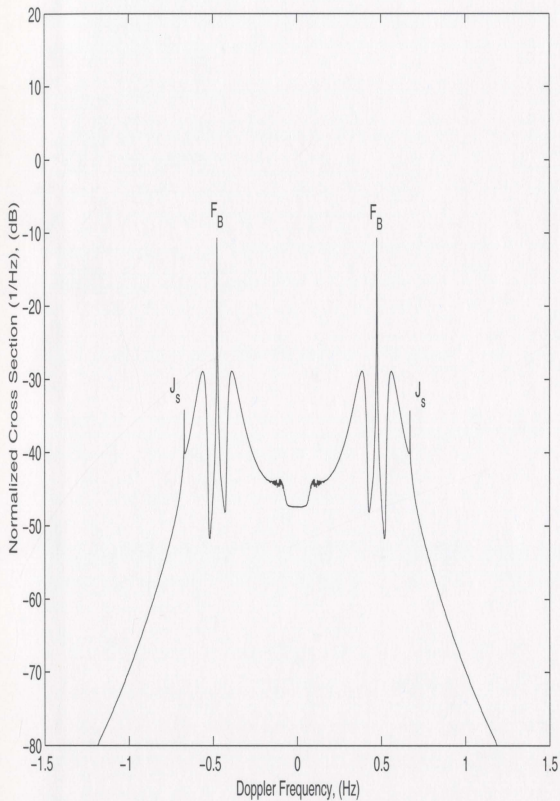


Figure 2.5: The combination of bistatic first- and second-order cross sections of the patch scatter. The radar operating frequency is 25 MHz, wind speed is 15m/s, wind direction is  $0^\circ$ , and bistatic angle is  $30^\circ$ .

Another source of singularities is the electromagnetic coupling coefficient. Gill [12] shows that the electromagnetic coupling coefficient has singularities when

$$\vec{K}_{1n} \cdot [\vec{K}_{1n} - 2k_0\hat{\rho}_2] = 0 \quad (2.78)$$

or

$$\vec{K}_{2n} \cdot [\vec{K}_{2n} - 2k_0\hat{\rho}_2] = 0, \quad (2.79)$$

and that the greatest effect of the singularities will occur at

$$K_{1n} = K_{2n} \quad (2.80)$$

and

$$\eta = \pm 2^{\frac{3}{4}} \sqrt{\frac{[1 \pm \sin \phi_0]^{\frac{1}{2}}}{\cos \phi_0}}. \quad (2.81)$$

It should be noted that the  $\pm$  inside the radicand is independent of that outside; i.e., there are a total of four singularities corresponding to the four possible combinations of  $\pm$  (see Gill [11]).

There is no singularity in the hydrodynamic coupling coefficient.

Since the second-order cross section of patch scatter  $\sigma_{2p}$  is dominated by the second-order hydrodynamic interactions of the scattering waves, and when the water becomes shallower, the importance of the hydrodynamic coupling coefficient is increased significantly compared with electromagnetic coupling coefficient [21], only the hydrodynamic coupling coefficient is used in our analysis.

When the delta function constraint is solved for  $K_{1n} < K_{2n}$ , the angle of  $\theta_{\vec{K}_{1n}}$  is in

the range given by (see Gill [11])

$$\theta_N - \pi \leq \theta_{\vec{K}_{1n}} < \theta_N - \beta_1 \quad (2.82)$$

and

$$\theta_N + \beta_1 \leq \theta_{\vec{K}_{1n}} < \theta_N + \pi, \quad (2.83)$$

where  $\beta_1$  is

$$\beta_1 = \begin{cases} \cos^{-1} \left[ 2 \left( \frac{1}{\eta} \right)^2 \right]; & |\eta| > \sqrt{2} \\ 0; & |\eta| < \sqrt{2} \end{cases} \quad (2.84)$$

Then the angle  $\theta_{\vec{K}_{2n}}$  is obtained as

$$\theta_{\vec{K}_{2n}} = \begin{cases} \theta_N + \cos^{-1} \beta_2; & \theta_N - \pi \leq \theta_{\vec{K}_{1n}} \leq \theta_N - \beta_1 \\ \theta_N - \cos^{-1} \beta_2; & \text{otherwise} \end{cases} \quad (2.85)$$

with

$$\beta_2 = \frac{1 + K_{2n}^2 - K_{1n}^2}{2K_{2n}}. \quad (2.86)$$

After trivial calculation, simulated bistatic Doppler radar spectra are obtained and plotted in the following figures. Figure 2.6 depicts the geometry of bistatic patch scatter.

Figure 2.7 depicts the first- and second-order bistatic cross sections of patch scatter for different water depths. The depths of water,  $d = 100$  m (deep water), 10 m, and 5 m are chosen to illustrate the behavior of radar Doppler spectra. The radar operating frequency is 25 MHz. The wind velocity is 15 m/s,  $0^\circ$  to the  $x$ -axis.

Figure 2.8 depicts the bistatic cross sections with wind directions  $\theta_w / =$

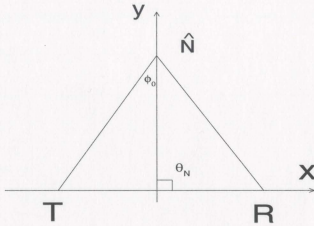


Figure 2.6: The geometry of bistatic patch scatter. The ellipse normal is  $90^\circ$ . Wind direction is indicated against the  $x$ -axis, Bistatic angle is  $30^\circ$ .

$0^\circ$ ,  $45^\circ$ ,  $90^\circ$ , and  $135^\circ$ . 25 MHz is used as the radar operating frequency. The wind directions of  $45^\circ$  and  $135^\circ$  are symmetrical with respect to the ellipse normal and produce identical results.

Figure 2.9 gives the bistatic cross sections for wind speeds of  $u = 10$  m/s. The radar operating frequency is 25 MHz. It is observed that the magnitude of the second-order cross section will increase significantly with increasing seastate.

Figure 2.10 depicts the bistatic first- and second-order cross sections for different radar operating frequencies. The same wind speed, wind direction, water depth and bistatic angle are used. Obviously, the Doppler shifts of the first-order peaks are different. In the second-order region, when the radar frequency is 25 MHz, the continuum adjacent to the Bragg peaks is clear and quite distinct. This means that much of the ocean spectral energy is mapped to these regions. When the radar frequency is 5.75 MHz, the second-order curve is not as distinct in the near Bragg regions because there is little spectral energy being mapped to the corresponding regions. The different behaviors of the second-order cross section in the near Bragg regions for higher and lower radar operating frequencies will significantly affect the inversion results as we will see in the next chapter.

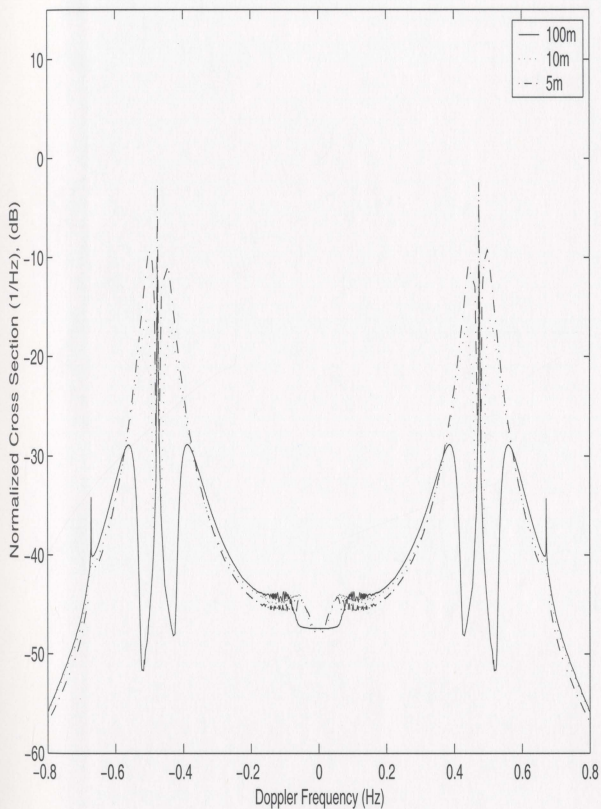


Figure 2.7: Bistatic second-order cross sections for water in different depths. The bistatic angle is  $\phi_0 = 30^\circ$ . The wind velocity is 15 m/s,  $0^\circ$  to the  $x$ -axis. The radar operating frequency is 25 MHz.

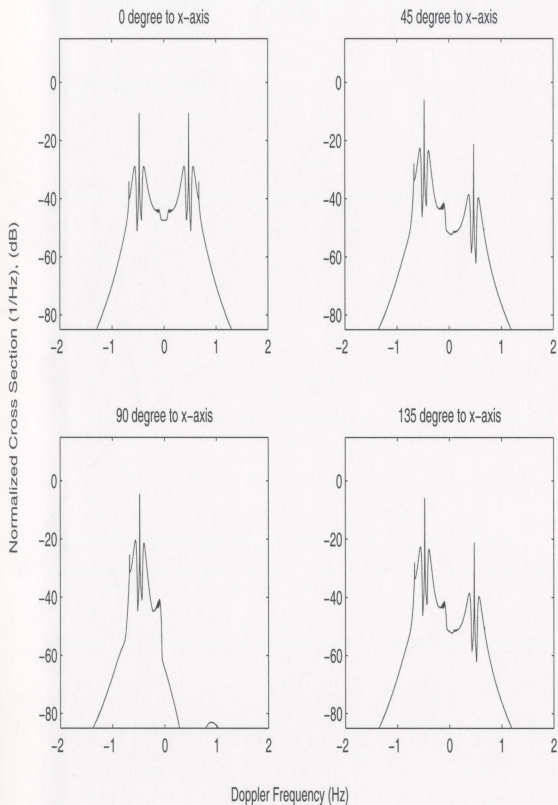


Figure 2.8: Bistatic second-order cross sections for a wind speed of 15 m/s and wind directions of  $\theta_w = 0^\circ, 45^\circ, 90^\circ,$  and  $135^\circ$ . The radar operating frequency is 25 MHz. Deep water is assumed.

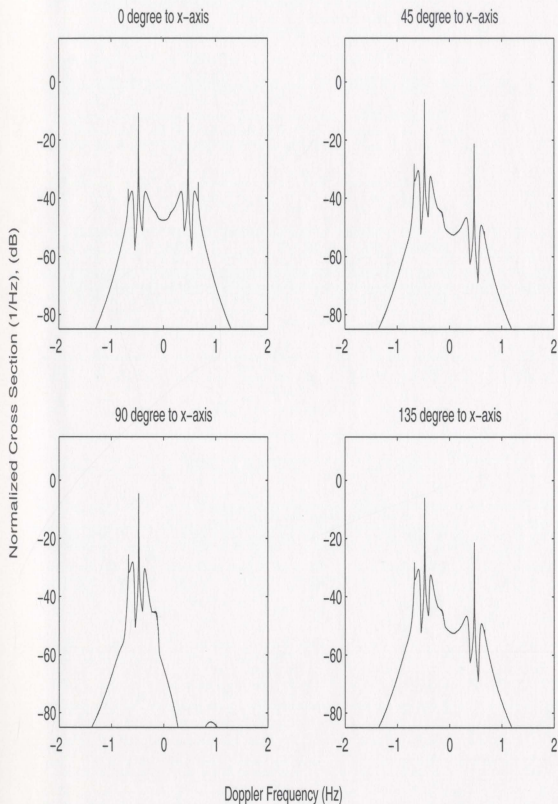


Figure 2.9: Bistatic second-order cross sections for wind speed in 10 m/s. The other parameters are kept consistent with Figure 2.8. Comparison of these two figures indicates the difference of the magnitude of the second-order cross sections.

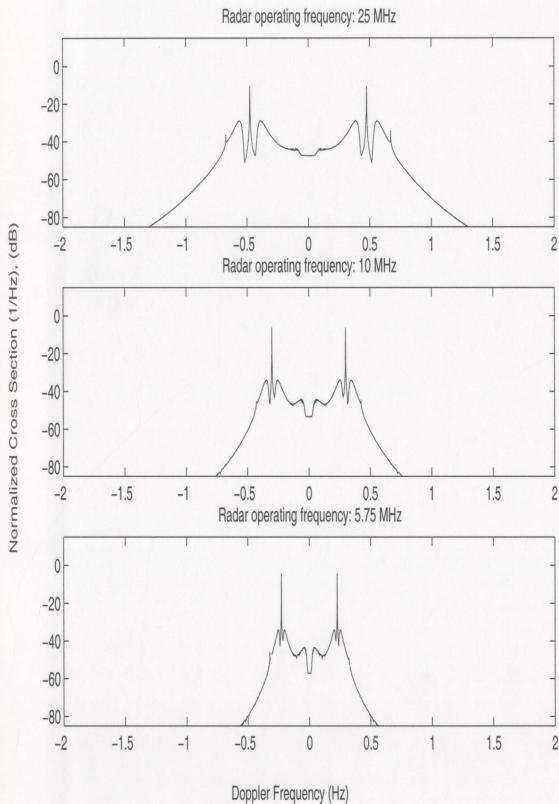


Figure 2.10: Bistatic second-order cross sections for radar operating frequencies are 25 MHz, 10 MHz, and 5.75 MHz. Wind speed is 15 m/s, deep water, the wind direction is parallel the reference direction.

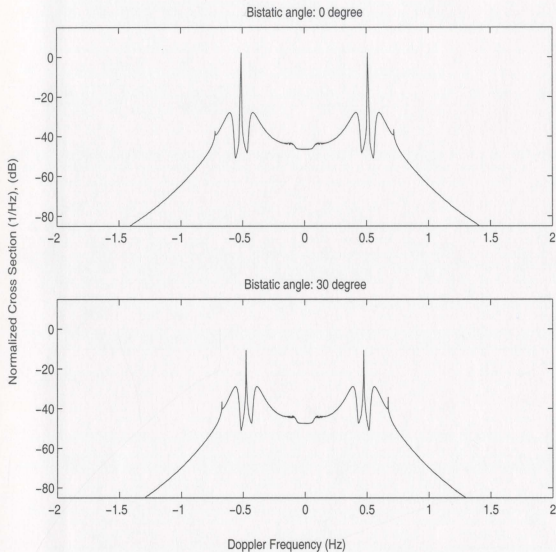


Figure 2.11: The cross sections for bistatic angles  $0^\circ$  (monostatic) and  $30^\circ$ . Wind speed is 15 m/s, the radar operating frequency is 25 MHz, deep water, the wind direction is  $0^\circ$  to the  $x$ -axis.

Figure 2.11 shows the comparison of the monostatic and bistatic cross section with bistatic angle  $\phi_0 = 30^\circ$ . All the other parameters are fixed. Comparing to the monostatic ( $\phi_0 = 0^\circ$ ) case, the entire cross section will be gradually reduced as the bistatic angle  $\phi_0$  approaches  $90^\circ$ . An explicit discussion involving this may be found in [12].

## Chapter 3

# Inversion of the Integral Equation

### 3.1 General

In this chapter, the integral equation of the second-order cross section is inverted to derive the non-directional ocean wave spectrum. The Doppler radar spectra are simulated according to the description of the last chapter. The influence from ocean currents is assumed to be zero. As a first step, the non-linear factor inside the integrand is linearized under the assumption that the selected Doppler frequency ranges are close to the first-order peaks. The corresponding ocean wave frequency ranges will contain the predominant portion of the ocean wave spectrum when the radar is operated in the upper half of the HF band.

The inversion of the integral equation is carried out numerically. A frequency band approximation is invoked to discretize the integral equation and the matrix equation is formed. The directional ocean wave spectrum is represented by a truncated Fourier series. Non-directional ocean wave spectra for different ocean conditions are derived and discussed.

## 3.2 Selection of the Ocean Wavenumber Range

The non-linearity of the integrand of the second-order cross section (see equation (2.59)) comes from the product of two unknown, but related factors,  $Z_1(m_1 \vec{K}_{1n})$  and  $Z_1(m_2 \vec{K}_{2n})$ . Lipa and Barrick [16] used the assumption that for  $K_{1n} < K_{2n}$ , the wave of  $\vec{K}_{2n}$  is in the saturated region of the ocean wave spectrum along with the Bragg wave. In this region, the magnitude of  $\vec{K}_{2n}$  will be approximately equal to the magnitude of Bragg wave  $\vec{K}_n$ . To specify the region, it is useful to define a dimensionless parameter,  $\mu$ , which is the magnitude of the normalized Doppler frequency shift from the first-order peaks and is given by

$$\mu = -m_1 (\eta + m_2) . \quad (3.1)$$

Within the range  $\mu < 0.4$ , the linear assumption is satisfied [16]. Howell [20] checked the difference between the directions of  $\vec{K}_{2n}$  and the Bragg peaks. This difference is denoted as  $\beta$ . He found that within the range of  $0.15 < \mu < 0.36$ , the maximum value of  $\beta$  would not exceed  $10^\circ$ . Thus, it is reasonable to replace the direction of  $\vec{K}_{2n}$  by the direction of Bragg wave, i.e., we may use  $\theta_N$  to represent  $\theta_{\vec{K}_{2n}}$ .

The range of  $\mu$  is used to determine the range of frequency that will be selected for the inverse analysis. From equation (3.1) and since  $m_1 = \frac{1}{m_1}$  for  $m_1 = \pm 1$ , we have

$$\eta = -m_1 \mu - m_2 . \quad (3.2)$$

If the range of  $\mu$  is known, so is the range of  $\eta$  for various combinations of  $m_1$  and  $m_2$ . In the algorithm that is described in this thesis, the range of  $\mu$  is selected as  $0.05 < \mu < 0.36$ , for region  $P_1$ ,  $m_1 = m_2 = 1$ . The range of frequency is  $-1.36 < \eta_{P_1} < -1.05$ . For part  $P_2$ ,  $m_1 = -1$ ,  $m_2 = 1$ . The range of frequency is  $-0.95 < \eta_{P_2} < -0.64$ . The ranges of the other two parts for  $m_1 = m_2 = -1$  and  $m_1 = 1$ ,  $m_2 = -1$ , are  $0.64 < \eta_{P_3} < 0.95$  and

$1.05 < \eta_{P_4} < 1.36$ , respectively.

Lipa and Barrick [16] provide a method to derive the boundaries of the corresponding wavenumber bands. Substituting the  $\eta$  of equation (2.58) into equation (3.1) and assuming deep water gives

$$\begin{aligned}\mu &= -m_1 \left( -m_1 \sqrt{K_{1n}} - m_2 \sqrt{K_{2n} + m_2} \right) \\ &= \sqrt{K_{1n}} + L \left( \sqrt{K_{2n} - 1} \right),\end{aligned}\quad (3.3)$$

where  $L = m_1 m_2$ . Since

$$K_{2n}^2 = K_{1n}^2 + 1 - 2K_{1n} \cos(\theta_{\bar{K}_{1n}} - \theta_N), \quad (3.4)$$

the maximum and minimum values of  $K_{2n}$  occur when

$$K_{2n} = \begin{cases} (K_{1n} + 1)^2, & \text{when } \theta_{\bar{K}_{1n}} = \pi + \theta_N \\ (K_{1n} - 1)^2, & \text{when } \theta_{\bar{K}_{1n}} = \theta_N \end{cases} \quad (3.5)$$

Substituting  $K_{2n}$  from equation (3.5) into equation (3.3) gives the range of  $\mu$  as

$$\mu = \begin{cases} \sqrt{K_{1n}} + \sqrt{1 + K_{1n}} - 1, & \text{when } \theta_{\bar{K}_{1n}} = \pi + \theta_N \\ \sqrt{K_{1n}} + \sqrt{1 - K_{1n}} - 1, & \text{when } \theta_{\bar{K}_{1n}} = \theta_N \end{cases} \quad (3.6)$$

Solving equation (3.6) gives the range of  $K_{1n}$  associated with the values of  $\mu$ .

$$K_{1L} \approx \mu^2 - \mu^3 \quad (3.7)$$

and

$$K_{1U} \approx \mu^2 + \mu^3, \quad (3.8)$$

where  $K_{1L}$  and  $K_{1U}$  are denoted as the lower and upper limitations of the wavenumber band, respectively.

### 3.3 The Linearization Method

The linearization scheme requires that the wave vector  $\vec{K}_{2n}$  lie in the saturated region of ocean wave spectrum. Within this range, Howell [20] invoked a Phillips equilibrium spectrum  $F_p$  [15] to linearize the directional ocean wave spectrum  $Z_1(m_2\vec{K}_{2n})$ , i.e.,

$$F_p = \begin{cases} \frac{0.005}{K_2^4}, & K_2 \geq K_c = \frac{g}{K_B u^2} \\ 0, & K_2 < K_c \end{cases} \quad (3.9)$$

and

$$Z_1(m_2\vec{K}_{2n}) = \frac{Z(m_2\hat{K}_{Bn})}{K_{2n}^4}. \quad (3.10)$$

Here  $K_{Bn}$  is the normalized Bragg wavenumber. Obviously,  $\hat{K}_{Bn} = 1$ . For  $K_1 < K_2$ , the value of  $m_2$  is always equal to the value of  $m$  in the first-order cross section.

Gill [23] suggested an alternate linearization scheme and obtained more precise results. In this scheme, the non-directional wave spectra,  $Z_1(m_1\vec{K}_{1n})$  and  $Z_1(m_2\vec{K}_{2n})$  are represented by the Fourier coefficients; i.e.

$$Z_1(m_1\vec{K}_{1n}) = \frac{1}{2\pi} \sum_{n_1=0}^{\infty} [a_{n_1}(K_{1n}) \cos(n_1\theta_{1n}) + b_{n_1}(K_{1n}) \sin(n_1\theta_{1n})] \quad (3.11)$$

and

$$Z_1(m_2\vec{K}_{2n}) = \frac{1}{2\pi} \sum_{n_2=0}^{\infty} [a_{n_2}(K_{2n}) \cos(n_2\theta_{2n}) + b_{n_2}(K_{2n}) \sin(n_2\theta_{2n})]. \quad (3.12)$$

Since the non-directional wave spectra are even functions of wind direction only the cosine terms of Fourier coefficients are needed in the expansions. Then, equations (3.11) and (3.12) are simplified as

$$Z_1(m_1 \vec{K}_{1n}) = \frac{1}{2\pi} \sum_{n=0}^{\infty} [a_n(K_{1n}) \cos(n\theta_{1n})] \quad (3.13)$$

and

$$Z_1(m_2 \vec{K}_{2n}) = \frac{1}{2\pi} \sum_{n=0}^{\infty} [a_n(K_{2n}) \cos(n\theta_{2n})], \quad (3.14)$$

respectively. Using the linearization scheme,  $a_n(K_{2n})$  in equation (3.14) is converted to the corresponding Fourier coefficients

$$a_n(K_{2n}) = \frac{a_n(K_{Bn})}{K_{2n}^4}, \quad (3.15)$$

where  $K_{Bn} = 1$ .

A linearized second-order bistatic cross section may be written from equation (2.59) and equation (3.15) as

$$\begin{aligned} \sigma_{2pmL}(\eta) = & 2 \sum_{m_1=\pm 1} \sum_{m_2=\pm 1} \int_{-\pi}^{\pi} \sum_{n_1=0}^{\infty} \sum_{n_2=0}^{\infty} [a_{n_1}(K_{1n}) \cos(n_1\theta_{\vec{K}_{1n}})] \\ & \cdot [a_{n_2}(1) \cos(n_2\theta_{\vec{K}_{2n}})] |S\Gamma_{pm}|^2 J_{tm} \frac{K_{1n}^{\frac{3}{2}}}{K_{2n}^4} d\theta_{\vec{K}_{1n}}. \end{aligned} \quad (3.16)$$

Here,  $\sigma_{2pmL}(\eta)$  denotes the linearized version of the second-order cross section of patch scatter. However, the upper limits of  $n_1$  and  $n_2$  cannot be calculated numerically, so a truncation value of 2 is used following the suggestion of previous investigators (see for

example, [20]). Equation (3.16) is rewritten as

$$\begin{aligned} \sigma_{2pnL}(\eta) = & 2 \sum_{m_1=\pm 1} \sum_{m_2=\pm 1} \int_{-\pi}^{\pi} \sum_{n_1=0}^2 \sum_{n_2=0}^2 \left[ a_{n_1}(K_{1n}) \cos(n_1 \theta_{\vec{K}_{1n}}) \right] \\ & \cdot \left[ a_{n_2}(1) \cos(n_2 \theta_{\vec{K}_{2n}}) \right] |S\Gamma_{pn}|^2 J_{tn} \frac{K_{1n}^{\frac{3}{2}}}{K_{2n}^4} d\theta_{\vec{K}_{1n}} \end{aligned} \quad (3.17)$$

with the Fourier coefficients being

$$a_{n_1}(K_{1n}) = \int_0^{2\pi} Z(m_1 \vec{K}_{1n}) \cos(n_1 \theta_{\vec{K}_{1n}}) d\theta_{\vec{K}_{1n}} . \quad (3.18)$$

For  $n_1 = 2$  we have

$$a_0(K_{1n}) = \int_0^{2\pi} Z(m_1 \vec{K}_{1n}) d\theta_{\vec{K}_{1n}} , \quad (3.19)$$

$$a_1(K_{1n}) = \int_0^{2\pi} Z(m_1 \vec{K}_{1n}) \cos(\theta_{\vec{K}_{1n}}) d\theta_{\vec{K}_{1n}} , \quad (3.20)$$

and

$$a_2(K_{1n}) = \int_0^{2\pi} Z(m_1 \vec{K}_{1n}) \cos(2\theta_{\vec{K}_{1n}}) d\theta_{\vec{K}_{1n}} . \quad (3.21)$$

The Fourier coefficient  $a_0(K_{1n})$  is of particular importance for the inverse problem. Comparing equation (3.19) with equation (2.69), we can see that

$$a_0(K_{1n}) = S_1(K) . \quad (3.22)$$

Thus the non-directional ocean wave spectrum will be recovered by finding the  $a_0$  coefficients.

The linearized Fourier coefficients,  $a_0(1)$ ,  $a_1(1)$ , and  $a_2(1)$  will be calculated by using

the first-order cross section. Barrick and Lipa [22] provided a set of expressions that may be used to calculate the Fourier coefficients from the directional wave spectrum.

$$a_0(k) = S(k) , \quad (3.23)$$

$$a_1(k) = S(k) \frac{2s}{s+1} \cos(\alpha^*) , \quad (3.24)$$

and

$$a_2(k) = S(k) \frac{2s(s-1)}{(s+1)(s+2)} \cos(2\alpha^*) . \quad (3.25)$$

When  $s = 2$  and  $k = 1$ , equations (3.23) – (3.25) become,

$$a_0(1) = S(1) , \quad (3.26)$$

$$a_1(1) = \frac{4S(1)}{3} \cos(\alpha^*) , \quad (3.27)$$

and

$$a_2(1) = \frac{S(1)}{3} \cos(2\alpha^*) . \quad (3.28)$$

where  $\alpha^*$  denotes the dominant direction of the wave field [21]. In our analysis, this direction is assumed to be equal to the wind direction. The wind direction may be ambiguously derived from the ratio of energy (obtained from equation (2.38)) in the left and right peaks of the first-order cross section.

### 3.4 Discretization of the Integral Equation

The discretization of the integral equation results in a summation. As we can see from the expression for the cross section in equation (3.17), for each value of  $\eta$ ,  $K_{1n}$  changes with the angle  $\theta_{\bar{K}_{1n}}$ . To discretize the integral, the continuous wavenumber values are separated into bands of equal size. The wavenumbers are assumed constant within a given band, with the central value being used as the representative wavenumber. This is the wavenumber band approximation suggested by Lipa and Barrick [16]. For each wavenumber band, the ocean wave spectrum can be represented by its corresponding Fourier series component. The integral is obtained by calculating the summation of values inside each wavenumber band.

Let  $J$  be the number of total wavenumber bands from  $K_1, K_2, \dots, K_j, \dots, K_J$ . The boundaries of the wavenumber bands are obtained from equation (3.7) and equation (3.8). The wavenumbers for each band are equally spaced.

For a specific wave frequency point  $\eta = \eta_s$ ,  $\theta_{\bar{K}_{1n}}$  changes from  $\theta_L$  to  $\theta_U$ . The related set of scattering wavenumbers is calculated. Each wavenumber belongs to a certain wavenumber band. There are  $Q$  wavenumber bands, where  $Q \leq J$ , associated with each  $\eta_s$ . For the  $a_0$  coefficient of the Fourier series, we have

$$\begin{aligned} \sigma_{2pL}(\eta_s)|_{a_0} = & \sum_{m_1=\pm 1} [a_0(m_1, K_{1n1}) F_{a_01} + a_0(m_1, K_{1n2}) F_{a_02} \\ & + \dots + a_0(m_1, K_{1nq}) F_{a_0q} \\ & + \dots + a_0(m_1, K_{1nQ}) F_{a_0Q}] , \end{aligned} \quad (3.29)$$

where  $F_{a_0q}$  is defined as

$$F_{a_0q} = 2 \sum_{m_2=\pm 1} \sum_{n_2=0}^2 \int_{\theta_{q-1}}^{\theta_q} [a_{n_2}(m_2, 1) \cos(n_2 \theta_{\bar{K}_{2n}})] |S\Gamma_{pm}|^2 J_{ln} \frac{K_{1n}^{\frac{3}{2}}}{K_{2n}^{\frac{3}{2}}} d\theta_{\bar{K}_{1n}} . \quad (3.30)$$

The second-order cross section contains four parts,  $P_1$ ,  $P_2$ ,  $P_3$ , and  $P_4$ , corresponding to the four combinations determined by  $m_1$  and  $m_2$  (see Figure 2.4). As noted in Section 3.3, it is convenient to denote the groups of the selected normalized Doppler frequencies by  $\mu$  where each  $\mu$  determines four Doppler frequencies from the four portions of the cross section. Letting the total number of  $\mu$  be  $I$  means that  $4I$  values of  $\eta$  are being used. Consequently, the integral equation of the linearized second-order cross section may be represented by a matrix equation

$$\underline{C} \cdot \underline{X} = \underline{B}, \quad (3.31)$$

where  $\underline{X}$  is a column array with its elements as the Fourier coefficients corresponding for each wave frequency band; i.e.

$$\underline{X} = \begin{bmatrix} 1x \\ 2x \\ \vdots \\ jx \\ \vdots \\ Jx \end{bmatrix} \quad (3.32)$$

with the element  $jx$  being

$$jx = \begin{bmatrix} ja_0(K_{1n}) \\ ja_1(K_{1n}) \\ ja_2(K_{1n}) \end{bmatrix}. \quad (3.33)$$

$\underline{B}$  is a column array with its elements being the simulated radar data selected for inversion

and may be represented as

$$\underline{B} = \begin{bmatrix} B(\mu_1) \\ B(\mu_2) \\ \vdots \\ B(\mu_i) \\ \vdots \\ B(\mu_I) \end{bmatrix}, \quad (3.34)$$

where the term  $B(\mu_i)$  contains the  $i^{\text{th}}$  set of four cross section components as indicated by

$${}_i B(\mu_i) = \begin{bmatrix} {}_i \sigma(\eta_{P1}) \\ {}_i \sigma(\eta_{P2}) \\ {}_i \sigma(\eta_{P3}) \\ {}_i \sigma(\eta_{P4}) \end{bmatrix}. \quad (3.35)$$

Matrix  $\underline{C}$  is denoted as the kernel matrix equation. Its  $4I$  number of rows corresponds to the number of selected frequencies. The number of columns is equal to the number of frequency bands  $J$  times the number of the Fourier coefficients. Then, the kernel matrix of  $\underline{C}$  has a dimension of  $4I \times 3J$ .

The arrangement of elements in the kernel matrix  $\underline{C}$  is critical to the stability of the subsequent inversion. Gill [21] suggested that the rows of matrix  $\underline{C}$  should be arranged according to increasingly large values of  $||\eta| - 1|$ ; i.e. the values of the cross section that are nearer the first-order peaks will be appear in the upper rows. Gill [21] also suggested that the zero-elements in the matrix  $\underline{C}$  should be *grouped* to avoid the energy spreading

throughout the matrix.

$${}_{i,j}C = \begin{bmatrix} \left( \int_{P_1,ij} F_{a_0ij} d\theta_{\bar{K}_{1n}} \right) & \left( \int_{P_1,ij} F_{a_{1ij}} d\theta_{\bar{K}_{1n}} \right) & \left( \int_{P_1,ij} F_{a_{2ij}} d\theta_{\bar{K}_{1n}} \right) \\ \left( \int_{P_2,ij} F_{a_0ij} d\theta_{\bar{K}_{1n}} \right) & \left( \int_{P_2,ij} F_{a_{1ij}} d\theta_{\bar{K}_{1n}} \right) & \left( \int_{P_2,ij} F_{a_{2ij}} d\theta_{\bar{K}_{1n}} \right) \\ \left( \int_{P_3,ij} F_{a_0ij} d\theta_{\bar{K}_{1n}} \right) & \left( \int_{P_3,ij} F_{a_{1ij}} d\theta_{\bar{K}_{1n}} \right) & \left( \int_{P_3,ij} F_{a_{2ij}} d\theta_{\bar{K}_{1n}} \right) \\ \left( \int_{P_4,ij} F_{a_0ij} d\theta_{\bar{K}_{1n}} \right) & \left( \int_{P_4,ij} F_{a_{1ij}} d\theta_{\bar{K}_{1n}} \right) & \left( \int_{P_4,ij} F_{a_{2ij}} d\theta_{\bar{K}_{1n}} \right) \end{bmatrix}, \quad (3.36)$$

where  $F_{a_0ij}$ ,  $F_{a_{1ij}}$ , and  $F_{a_{2ij}}$  are of the form of the expressions in equation (3.30). The numerical simulation has validated this construction of  $\underline{C}$ . A subroutine function of *Matlab* [29], *FreqBand.m*, is carried out for the arrangement. This is an effective but not unique way to arrange the elements of  $\underline{C}$ . The number of frequency bands,  $J$ , is chosen as 60 and the Fourier series representation is truncated as  $n = 0, 1$ , and 2. Thus, the number of columns of  $\underline{C}$  is  $3J = 180$ . The number of selected frequency groups are approximately  $\mu = 120$ , giving the matrix  $\underline{C}$  to have a dimension of  $480 \times 180$ .

### 3.5 SVD Solution of the Matrix Equation

Ideally, the problem of solving a matrix equation such as (3.31) means determining

$$\underline{X} = \underline{C}^{-1} \underline{B}, \quad (3.37)$$

where  $\underline{C}^{-1}$  is the inverse of  $\underline{C}$ . In this solution,  $\underline{X}$  can be extracted precisely and uniquely providing  $\underline{C}^{-1}$  exists. However, in the most general situation, the inverse matrix  $\underline{C}^{-1}$  may not exist. In that case, there will be no unique solution for  $\underline{X}$ . The matrix equation is then denoted to be singular. However, this kind of matrix equation may still be solved approximately. Instead of finding the inverse matrix  $\underline{C}^{-1}$ , the singular value decomposition (SVD) method (e.g. see Stewart [30]) is invoked to find a pseudo-inverse matrix  $\underline{C}^+$

for kernel matrix  $\underline{C}$ . Then,

$$\underline{X} = \underline{C}^+ \underline{B}. \quad (3.38)$$

The solution of  $\underline{X}$  is denoted as a *linear least squares solution*.

For any real  $(n \times m)$  matrix  $\underline{C}$ , there exists orthogonal matrices  $\underline{U}$  and  $\underline{V}$ , with dimensions  $m \times m$  and  $n \times n$ , respectively, which satisfy,

$$\underline{U}^T \underline{C} \underline{V} = \begin{bmatrix} \Sigma & \dots & 0 \\ \vdots & \ddots & \vdots \\ 0 & \dots & 0 \end{bmatrix}, \quad (3.39)$$

where  $\underline{U}^T$  is the transpose of  $\underline{U}$  and  $\Sigma$  is a diagonal matrix with non-zero, positive elements,  $\mu_1, \mu_2, \dots, \mu_n$  satisfying

$$\mu_1 \geq \mu_2 \geq \dots \mu_n \geq 0. \quad (3.40)$$

These elements,  $\mu_1, \mu_2, \dots, \mu_n$ , are referred to as the singular values of  $\underline{C}$ . The columns of matrix  $\underline{U}$  are the so-called right singular vectors of  $\underline{C}$  and the columns of  $\underline{V}$  are the so-called left singular vectors of  $\underline{C}$ . Specifically, if the matrix  $\underline{C}$  were not singular, the *pseudo-inverse* of  $\underline{C}$  would be equal to  $\underline{C}^{-1}$ . The elements inside the diagonal matrix  $\Sigma$  are the eigenvalues of  $\underline{C}$ . From equation (3.39),  $\underline{C}^+$  is

$$\underline{C}^+ = \underline{V} \begin{bmatrix} \Sigma^{-1} & \dots & 0 \\ \vdots & \ddots & \vdots \\ 0 & \dots & 0 \end{bmatrix} \underline{U}^T. \quad (3.41)$$

A *Matlab* [29] function, *svd*, is invoked to calculate the singular values of  $\underline{C}$  in order to obtain  $\underline{C}^+$ . The rank of  $\underline{C}$  is also derived to show the number of linearly independent

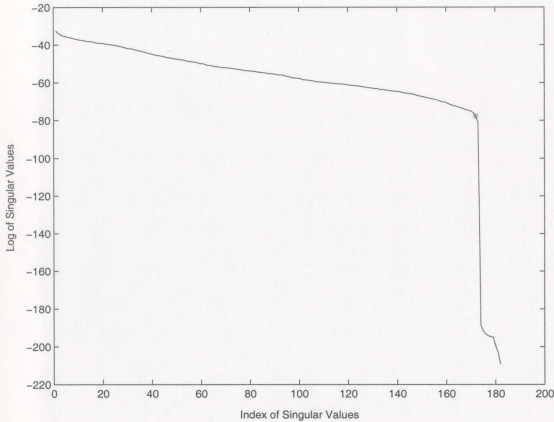


Figure 3.1: A example of the choice of the retained number of singular values. The rank of the kernel matrix is located by a “\*” with a value of  $r = 172$ . The radar frequency is 25 MHz. The wind speed is 15 m/s and the wind direction is zero degrees to the  $x$ -axis.

terms in  $\underline{C}$ .  $a_0(K_{1n})$  is obtained from the solution of  $\underline{X}$  as the ocean wave non-directional spectrum. The results are discussed in the next section.

The determination of how many of the singular values of the kernel matrix  $\underline{C}$  should be retained is another important issue. Beyond a certain number, the singular values will be truncated because they decrease significantly in magnitude and introduce instability in the inversion process. This problem has been well investigated by Howell [20]. Generally speaking, the retained number, denoted as  $r$ , is chosen as a number equal to or less than the rank of the matrix. In our programming, the value  $r$  is selected to be equal to rank of matrix  $\underline{C}$ . Figure 3.1 depicts a typical behaviour of the singular values. The retained number  $r = 172$  is denoted by a “\*”.

## 3.6 Illustration of the Results

### 3.6.1 Recovery of Ocean Wave Spectra

From the inverse analysis described in this chapter ocean wave spectra are obtained. For the purpose of illustration, the bistatic angle is fixed at  $30^\circ$ . The scattering ellipse normal is  $90^\circ$  (see Figure 2.6). Several sets of plots, corresponding to different water depths, wind directions, wind speeds, and radar frequencies are obtained and shown.

Figure 3.2 is for different water depths. The radar frequency is  $f_0 = 25$  MHz, wind speed is 15 m/s, and the wind direction is  $0^\circ$  to  $x$ -axis. The shallow water effect will be observed when the water depth is less than 10 m. The bias in magnitude and shape are more significant when water depth is lower than 5 m because of the influence from the seafloor. This effect results in a hyperbolic function in the cross section.

Figure 3.3 depicts the recovered non-directional spectra for wind directions  $\theta_w$  equal to  $0^\circ$ ,  $45^\circ$ ,  $90^\circ$ , and  $135^\circ$  to the  $x$ -axis and the wind speed of 15 m/s. The radar frequency is  $f_0 = 25$  MHz and the water is deep. When the wind directions are not equal to  $90^\circ$ , the inversion results are well matched with the ideal Pierson-Moskowitz non-directional spectrum in shapes and magnitudes. When the wind direction  $\theta_w$  is equal to  $90^\circ$ , which means the wind direction is perpendicular to the  $x$ -axis, this match is significantly reduced since, as shown by Figure 2.9 in Chapter 2, only one-half of the cross section data can be used to recover the ocean wave spectrum.

Figure 3.4 depicts the recovered ocean wave spectra for wind directions  $\theta_w$  are  $0^\circ$ ,  $45^\circ$ ,  $90^\circ$ , and  $135^\circ$  to the  $x$ -axis while the wind speed is 10 m/s. The other parameters are the same as for Figure 3.3. The similar results are obtained; however, the recovered shapes do not agree with ideal non-directional spectrum as much as when the wind speed is 15 m/s since for lower seastate, the assumption for linearization is not as good [21].

Figure 3.5 depicts the results for different radar frequencies. HF band frequencies

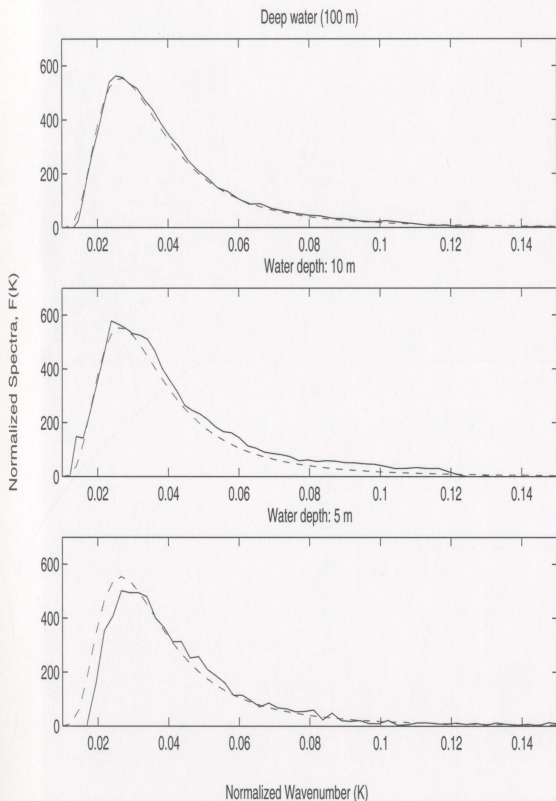


Figure 3.2: Comparison of spectra from inversion (solid line) with Pierson-Moskowitz model (dashed line) for different water depths. Radar frequency is 25 MHz. The wind speed is 15 m/s and the wind direction is  $0^\circ$  to the  $x$ -axis.

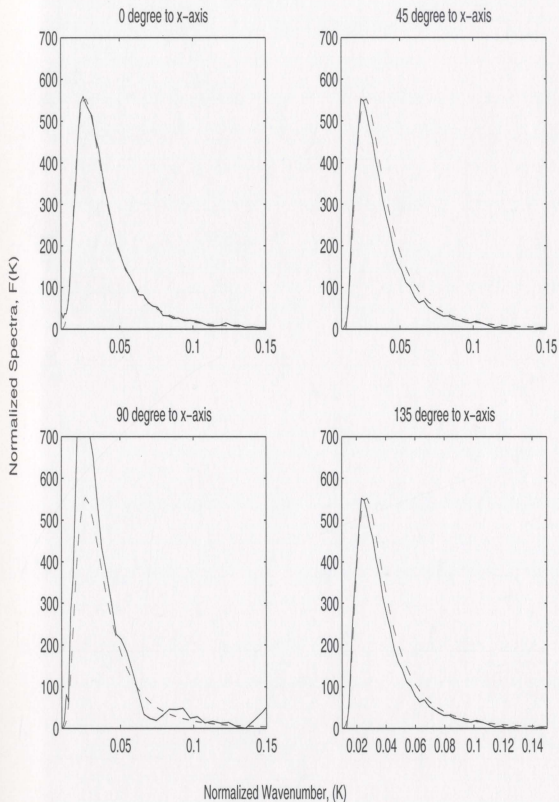


Figure 3.3: Comparison of spectra from inversion (solid line) with Pierson-Moskowitz model (dashed line) for different wind directions. The water is deep. The radar frequency is 25 MHz. The wind speed is 15 m/s.

25 MHz, 10 MHz, and 5.75 MHz are used and the results are compared. It is observed that almost all the non-directional ocean wave spectrum is recovered from the Doppler spectrum for a radar frequency of 25 MHz, i.e., the upper level of the HF band. However, for the lower level of the HF frequency band, such as 10 MHz and 5.75 MHz, the higher part of the non-directional spectrum is not available. This phenomenon may be explained from equations (3.7) and (3.8). These two equations give the normalized lower ( $K_{1L}$ ) and upper ( $K_{1U}$ ) wavenumber boundaries of the recovering spectrum. Since  $\mu$  is selected in the range  $0.05 < \mu < 0.36$ ,  $K_{1L}$  will be

$$K_{1L} = 0.05^2 - 0.05^3 = 0.0024, \quad (3.42)$$

and  $K_{1U}$  will be

$$K_{1U} = 0.36^2 + 0.36^3 = 0.176. \quad (3.43)$$

When the normalized wavenumbers  $K_{1L}$  and  $K_{1U}$  are converted to the non-normalized versions, they will be multiplied by the factor  $2k_0 \cos(\phi_0)$ , which is a function of radar operating frequency and the bistatic angle. Let  $\phi_0 = 30^\circ$ , for radar frequency at 25 MHz, the range of recovered wavenumber may be  $0.0022 < k_1 < 0.160$ . For 10 MHz, the range of wavenumber may be  $0.0008 < k_1 < 0.064$ , and for 5.75 MHz the range is  $0.0005 < k_1 < 0.037$ . The recovered wavenumber ranges are reduced when radar frequencies are decreased. This fact suggests that the optimal operating frequencies for the purposes of radio wave oceanographs lie in the upper HF band (20 – 30 MHz).

### 3.6.2 Normalized RMS Waveheight

The normalized *rms* waveheights corresponding to Figures 3.2 – 3.5 are listed in Tables 3.1 – 3.4. The *rms* waveheight values extracted directly from a Pierson-Moskowitz wave

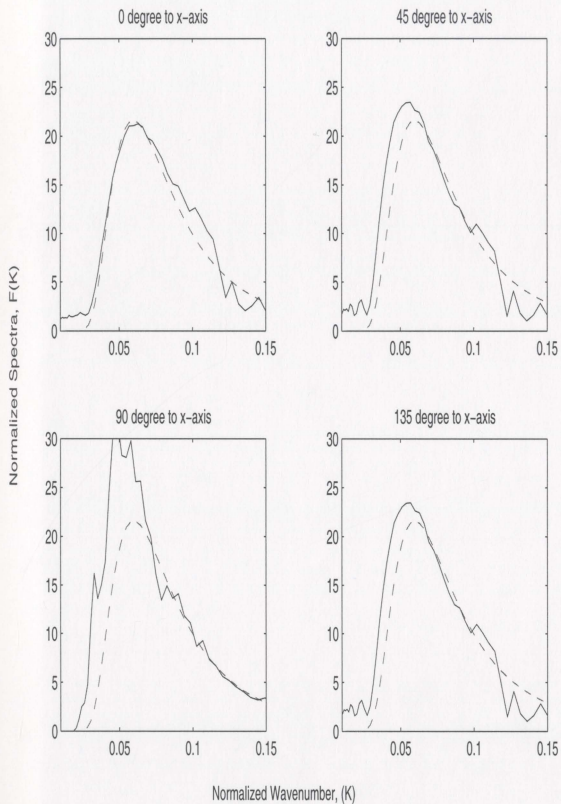


Figure 3.4: Comparison of spectra from inversion (solid line) with Pierson-Moskowitz model (dashed line) for different wind directions. The water is deep. The radar frequency is 25 MHz. The wind speed is 10 m/s.

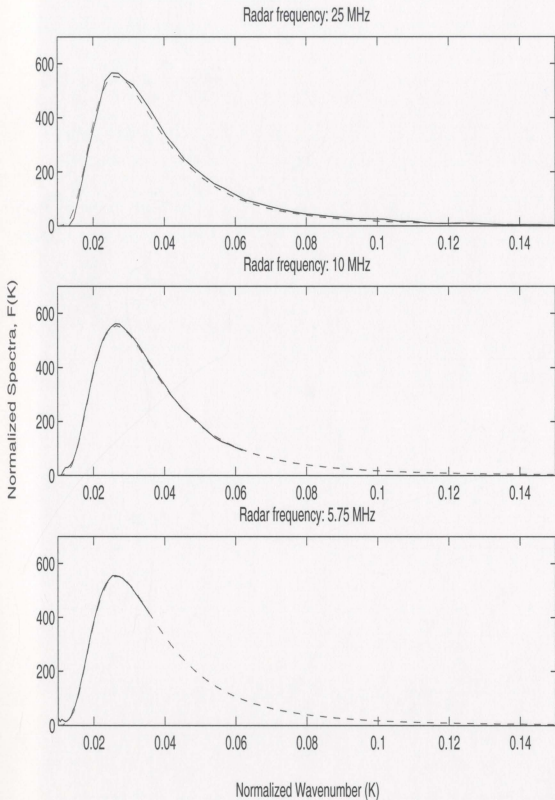


Figure 3.5: Comparison of spectra from inversion (solid line) with Pierson-Moskowitz model (dashed line) for different radar frequencies. The water is deep. The wind speed is 15 m/s and the wind direction is  $0^\circ$  to the  $x$ -axis.

model are tabulated simultaneously for comparison. According to Lipa and Barrick [19] the normalized *rms* waveheight is

$$H^2 = \int_0^\infty \int_{-\pi}^\pi K Z(\vec{K}) d\theta dK . \quad (3.44)$$

When  $Z(\vec{K})$  is represented by the first three Fourier coefficients, equation (3.44) becomes

$$H^2 = \int_0^\infty K a_0(K) dK . \quad (3.45)$$

where  $a_0$  is the zero-order Fourier coefficient of ocean wave spectrum. An equation of numerical calculation of *rms* waveheight is, Gill [21],

$$\begin{aligned} H^2 \approx & \int_{K_1}^{K_2} K a_0(K_{m1}) dK + \dots + \int_j^{K_{j+1}} K a_0(K_{mj}) dK \\ & + \dots + \int_j^{K_{j+1}} K a_0(K_{mj}) dK \\ & + \frac{K_2^2 - K_1^2}{2} a_0(K_{m1}) + \dots + \frac{K_{i+1}^2 - K_i^2}{2} a_0(K_{mi}) . \end{aligned} \quad (3.46)$$

Depths (m)	Model	Inversion	%Difference
100 (deep)	0.8424	0.8507	0.1
10	0.8365	0.8341	1.5
5	0.8370	0.8257	1.4

Table 3.1: Normalized Waveheights for Different Water Depths.

<i>Directions</i> (degree)	<i>Model</i>	<i>Inversion</i>	<i>%Difference</i>
0	0.8424	0.8457	0.4
45	0.8424	0.7733	8.2
90	0.8473	0.7991	5.7
135	0.8424	0.7733	8.2

Table 3.2: Normalized Waveheights for Different Wind Directions ( $\mu = 15$  m/s).

<i>Directions</i> (degree)	<i>Model</i>	<i>Inversion</i>	<i>%Difference</i>
0	0.3289	0.3367	2.4
45	0.3289	0.3282	0.2
90	0.3289	0.3527	7.2
135	0.3289	0.3282	0.2

Table 3.3: Normalized Waveheights for Different Wind Directions ( $\mu = 10$  m/s).

<i>Frequencies</i> (MHz)	<i>Model</i>	<i>Inversion</i>	<i>%Difference</i>
25	0.8479	0.8696	0.4
10	0.8461	0.7178	15.2
5.75	0.8432	0.4880	42.1

Table 3.4: Normalized Waveheights for Different Radar Frequencies.

# Chapter 4

## Inverse Analysis for Noisy Spectra

### 4.1 General Introduction

The non-directional ocean wave spectrum is recovered from the bistatic cross section in the previous chapter. The input radar data are ideally simulated to build up the foundation of the analysis. Gill [12] presents a more realistic model to describe the received power from the ocean surface scatter. In that analysis, the power spectral densities (PSD) of the ocean clutter and ambient noise are obtained. The purpose of this chapter is to calculate the ocean wave spectrum based upon noisy radar returns.

The received PSD due to clutter is a function of radar transmitted power, the gains of the transmitter and receiver antennas, distance of the scattering patch, the operating frequency, the attenuation function associated with the characteristics of the medium, and the scattering cross section.

In the HF band, the external noise comes from a wide range of sources, such as atmospheric, galactic, and man-made noise. To remain consistent with previous investigations [12] the noise is assumed to be a stationary Gaussian white process with zero mean.

In this chapter, the PSDs of clutter and noise are calculated. The combination of clutter and noise in the time domain gives the time series of the radar received signal.

This signal is then transferred to the frequency domain to achieve the overall PSD of the radar signal. The inverse analysis described in the last chapter is applied to the simulated PSD of radar returns. Consequently, the non-directional ocean wave spectrum is recovered.

## 4.2 The PSD of Ocean Clutter

Before calculating the PSD of ocean clutter, the parameters of the radar transmitting and receiving systems must be specified. To keep our analysis consistent with [12], we use the parameters presented there. Obviously, these parameters, as listed below, may be altered for any practical utilization.

- radar operating frequency:  $f_0 = 25$  MHz, (i.e.  $\lambda_0 = 12$  m)
- peak power:  $P_t = 16$  kW
- transmitter gain:  $G_t = 2$  dBi  $\approx 1.585$
- receive array: 24 element linear array with element spacing  $d_s = \frac{\lambda_0}{2}$ , operating in the broadside mode
- receive array beam width: from Collin [31], the half-power beam width of an  $N + 1$  element broadside array is

$$BW_{\frac{1}{2}} = \frac{2.65\lambda_0}{(N + 1)\pi d_s} = 0.07029 \text{ rad } (4.03^\circ) \quad (4.1)$$

- receive array gain: assuming 100% efficiency, [31] gives

$$G_r = \frac{5.48(N + 1)d_s}{\lambda_0} = 65.76 \quad (4.2)$$

- the transmitting signal is considered as an infinite pulse train (Figure 4.1) with the pulse width:  $\tau_0 = 13.3 \mu\text{s}$  (the patch width in the simulation of the first-order cross

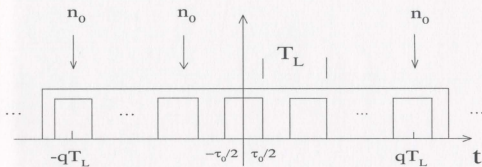


Figure 4.1: A pulse train with pulse width  $\tau_0$  and pulse repetition frequency  $T_L$ .  $n_0$  is the noise.

section is  $\Delta\rho_s = \frac{c\tau_0}{2} = 2000$  m).

- the pulse repetition frequency: prf = 3 kHz, i.e.  $T_L = 333 \mu s$  where  $T_L$  is the pulse repetition period.
- patch area:

$$Ar = \frac{c\tau_0\rho_{20}BW_{\frac{1}{2}}}{2} \quad (4.3)$$

where  $\frac{c\tau_0}{2}$  and  $\rho_{02}BW_{\frac{1}{2}}$  are the radial and azimuthal extents of the patch, respectively.

- normalized patch cross section:  $\sigma(\eta) = \sigma(\eta)_{11} + \sigma(\eta)_{2P}$  as calculated from Chapter 2 (see equation (2.34) and equation (2.59)).
- rough spherical earth attenuation functions:  $F(\cdot)$  are calculated from Dawe's [32] FORTRAN code. The distances from the radar transmitter to scattering patch and from the

scattering patch to receiver are chosen to be 50 km. The relative permittivity of ocean water is taken as 80. The average conductivity is 4 U/m.

The PSD of clutter from the ocean surface is given by

$$P_c(\eta) = \frac{\lambda_0^2 \left(\frac{\pi\sigma}{T_L}\right) P_t G_t G_r |F(\rho_{01}, \omega_0) F(\rho_{02}, \omega_0)|^2 A r \sigma(\eta)}{(4\pi)^3 \rho_{01}^2 \rho_{02}^2} . \quad (4.4)$$

It is emphasized here that this PSD is actually a Doppler clutter PSD for the ocean surface (see [12]).

### 4.3 The PSD of Stationary Gaussian Noise

Gill [12] presents a detailed description of the PSD of stationary Gaussian white noise. Since we want to keep our analysis consistent with his work, Gill's equations and definitions of parameters are quoted in this thesis. The external Doppler noise PSD  $P_N(\omega)$  is

$$P_N(\omega) = F(d) S_N(\omega') , \quad (4.5)$$

where  $\omega'$  is radar radian frequency ( $= 2\pi f'$ ), and the  $\omega$  is the radian Doppler frequency. For infinitely many pulses with the sampling at pulse center,  $F(d)$  factor has the form

$$F(d) = d \sum_{L(-\frac{1}{2d})}^{G(\frac{1}{2d})} Sa[m\pi d] , \quad (4.6)$$

where the quantity  $L\left(-\frac{1}{2d}\right)$  is the smallest integer that is greater than or equal to  $-\frac{1}{2d}$ , and  $G\left(\frac{1}{2d}\right)$  is the greatest integer that is less than or equal to  $\frac{1}{2d}$  and  $Sa(\cdot)$  is sampling function.

To derive the PSD  $S_N(\omega')$  of the ambient noise, an external noise factor,  $f_a$ , is found

as

$$f_a = \frac{P_n}{kT_0B_n}, \quad (4.7)$$

where  $P_n$  is the available noise power from an equivalent lossless antenna,  $k = 1.38 \times 10^{-23} J/K$  is Boltzmann's constant,  $T_0 = 290K$  is the reference temperature, and  $B_n$  is the noise power bandwidth of the receiving system. For a matched filter system,  $B_n$  may be taken as the reciprocal of transmit pulse width,  $\tau_0$ .

Commonly, an external noise figure,  $F_{am}$ , which is defined as

$$F_{am} = 10 \log f_a, \quad (4.8)$$

can be found from such documents as *ITU-R Recommendations*[33]. For a white noise process, the PSD of the ambient noise is

$$S_N(\omega') = \frac{P_n}{2\pi B_n}. \quad (4.9)$$

Evaluation of  $P_n$  from  $F_{am}$  gives the expression of the PSD of ambient noise as

$$S_N(\omega') = \frac{kT_0}{2\pi} 10^{\frac{F_{am}}{10}}. \quad (4.10)$$

Then, using equations (4.5), (4.6), and (4.10), the external Doppler noise spectral density,  $P_N(\omega)$ , becomes

$$P_N(\omega) = \frac{dKT_0}{2\pi} 10^{\left(\frac{F_{am}}{10}\right)} \sum_{L\left(-\frac{1}{2d}\right)}^{G\left(\frac{1}{2d}\right)} Sa[m\pi d]. \quad (4.11)$$

## 4.4 The Time Series of Radar Return and its PSD

The modeled Doppler PSD is the “sum” of ocean clutter and noise. This “sum” should be done first in the time domain. Using Pierson’s model [34] of a one-dimensional stationary Gaussian process, Gill [12] presents a time function  $f(t)$  of limited bandwidth  $B$  to describe the ocean wave system as

$$f(t) = \int_B e^{j\omega t} e^{j\epsilon(\omega)} \sqrt{F_s(\omega) \frac{d\omega}{2\pi}}, \quad (4.12)$$

where  $F_s(\omega)$  is power spectral density of  $f(t)$ . The frequency is defined in the range

$$-\frac{B}{2} \leq \omega \leq \frac{B}{2}. \quad (4.13)$$

The PSD of the clutter and noise, symbolized previously as  $P_c$  and  $P_N$ , respectively, may be transferred to the time domain by equation (4.12). The corresponding time series of clutter and noise are denoted as  $c(t)$  and  $n(t)$ , respectively. The sum of  $c(t)$  and  $n(t)$  gives the total simulated signal  $s(t)$  received by radar.

$$s(t) = c(t) + n(t). \quad (4.14)$$

However, the integral of equation (4.12) cannot be calculated directly. A summation representation is presented by Pierson [34] for numerical calculation.

$$f(t) = \lim_{\substack{\omega_{2p} \rightarrow \infty \\ (\omega_{2q+2} - \omega_{2q}) \rightarrow 0}} \sum_{q=0}^p e^{j(\omega_{2q+1}t)} e^{j\epsilon(\omega_{2q+1})} \sqrt{F_s(\omega_{2q+1}) \cdot \frac{\omega_{2q+2} - \omega_{2q}}{2\pi}}, \quad (4.15)$$

where  $q$  is whole number. When  $\omega_{2p} \rightarrow \infty$ , the number of pulse trains extends to infinity.

Bobby [35] provides the  $C^{++}$  code of the process defined in equation (4.15). The *Matlab* routine to accomplish the same process is given in Appendix A.

The simulated Doppler PSD of radar data is obtained by means of a *Matlab* [29] fast Fourier transformation function *fft*. A 512-point *fft* with 50% overlap and 15 averages are used to calculate the PSD spectrum. Figures 4.2 – 4.5 depict typical noisy radar Doppler PSD for different water depths, wind directions, wind speeds, and radar operating frequencies. Comparing with Figures 2.7 – 2.10 in Chapter 2, the ripples over the curve are observed because of the contamination by noise. When the wind speed is 10 m/s or lower and the wind direction is in an angle more than  $45^\circ$ , the second-order part of the positive Doppler PSD is hidden by noise.

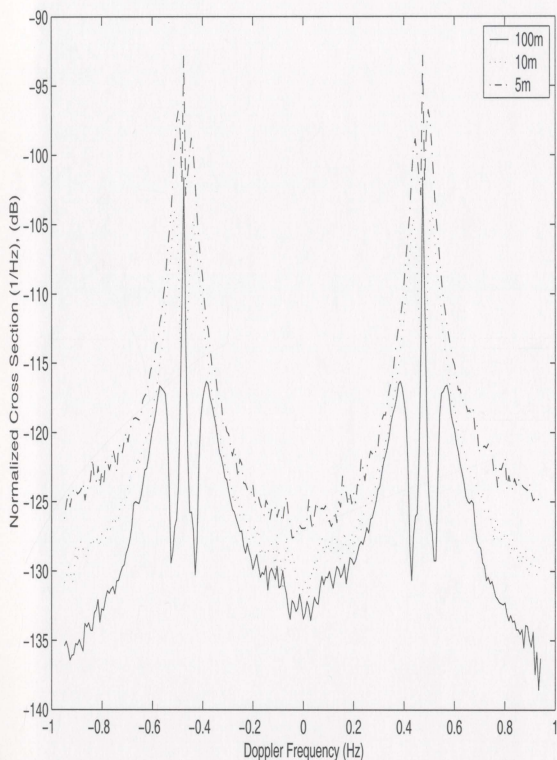


Figure 4.2: The simulated radar Doppler power spectral density (PSD) with zero-mean stationary Gaussian noise for water at different depths. The bistatic angle is  $\phi_0 = 30^\circ$ , the wind velocity is 15 m/s,  $0^\circ$  to the  $x$ -axis; the radar operating frequency is 25 MHz.

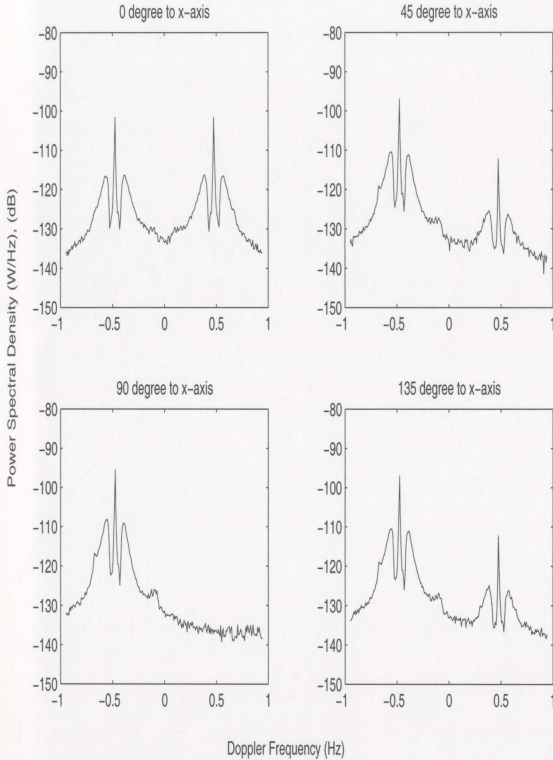


Figure 4.3: The simulated radar Doppler power spectral density (PSD) with zero-mean stationary Gaussian noise for wind speed of 15 m/s. The wind directions are  $\theta_w = 0^\circ, 45^\circ, 90^\circ,$  and  $135^\circ$ . The radar operating frequency is 25 MHz, bistatic angle is  $30^\circ$ , and deep water is assumed. Since  $45^\circ$  and  $135^\circ$  are symmetric with respect to the ellipse normal, we cannot tell the difference between them.

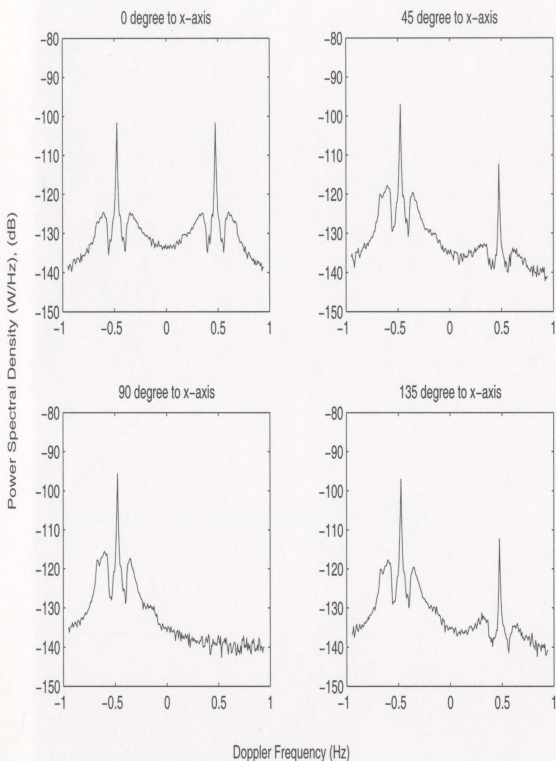


Figure 4.4: The simulated radar Doppler power spectral density (PSD) with zero-mean stationary Gaussian noise for a wind speed of 10 m/s. The other parameters are kept consistent with Figure 4.3. Comparison of these two figures indicates the difference of the magnitude of the second-order cross sections.

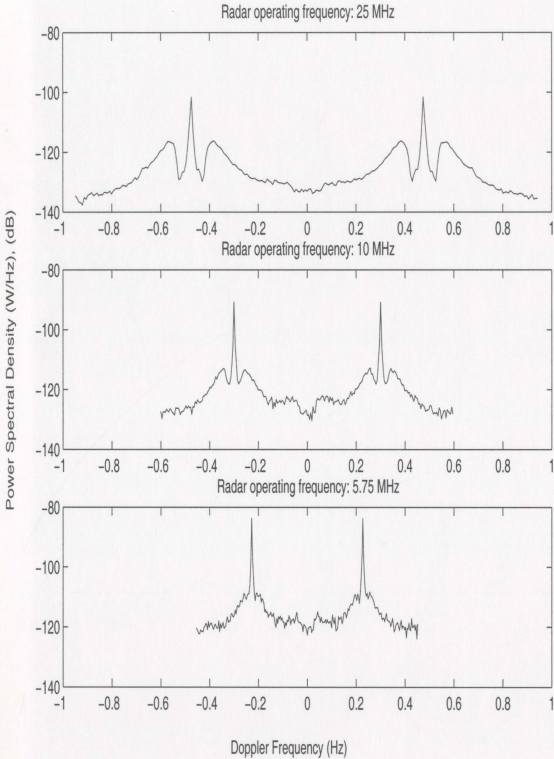


Figure 4.5: The simulated radar Doppler power spectral density (PSD) with different radar operating frequencies. Wind speed: 15 m/s, wind direction:  $0^\circ$  to  $x$ -axis, bistatic angle:  $30^\circ$ , and deep water.

## 4.5 The Inverse Analysis for Noisy Spectra

### 4.5.1 Recovery of Ocean Wave Spectra

The inverse analysis for noisy data uses the same procedure as explained in Chapter 3. The simulated radar data are produced according to the description in the previous section. Figures 4.6 – 4.9 depict recovered ocean wave spectra for different water depths, wind directions, wind speeds, and radar operating frequencies, associated with Figures 4.2 – 4.5.

### 4.5.2 Normalized RMS Waveheight

Normalized *rms* waveheights are also calculated for each ocean wave spectrum received. The resulting waveheights are tabulated in Tables 4.1 – 4.4 with comparison of the *rms* waveheight values extracted directly from a Pierson-Moskowitz wave model.

The comments about the inversion results in Chapter 3 may also be used here. It is obvious that the results from noisy spectra for non-directional wave spectra and normalized *rms* waveheights are less well matched to the actual conditions than those from noise-free spectra. As in Section 3.6, for some special wave field conditions, such as shallow water, lower seastate, and when the wind direction is  $90^\circ$  to the  $x$ -axis, the mis-matches appear to be more significant.

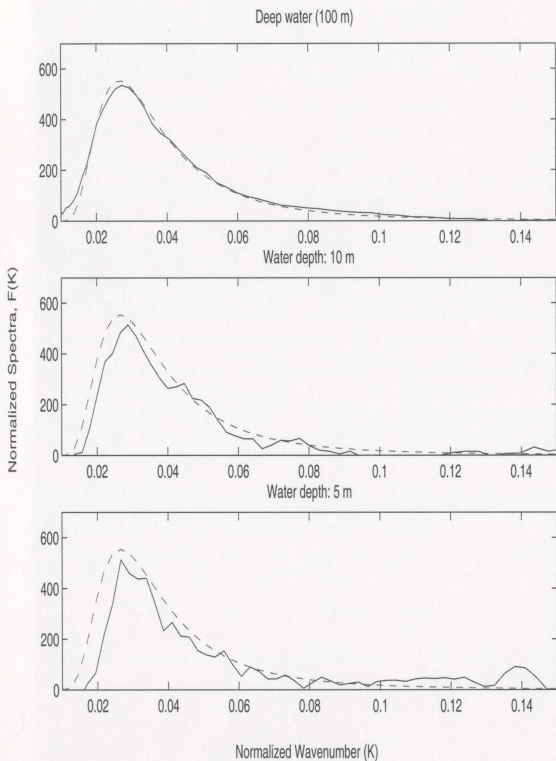


Figure 4.6: The recovered non-directional spectra from noisy radar Doppler PSD for different water depths. Radar frequency is 25 MHz, the wind speed is 15 m/s and the wind direction is zero degree to the  $x$ -axis. The solid lines are the wave spectra from inversion. The dashed lines are the spectra calculated by Pierson-Moskowitz model.

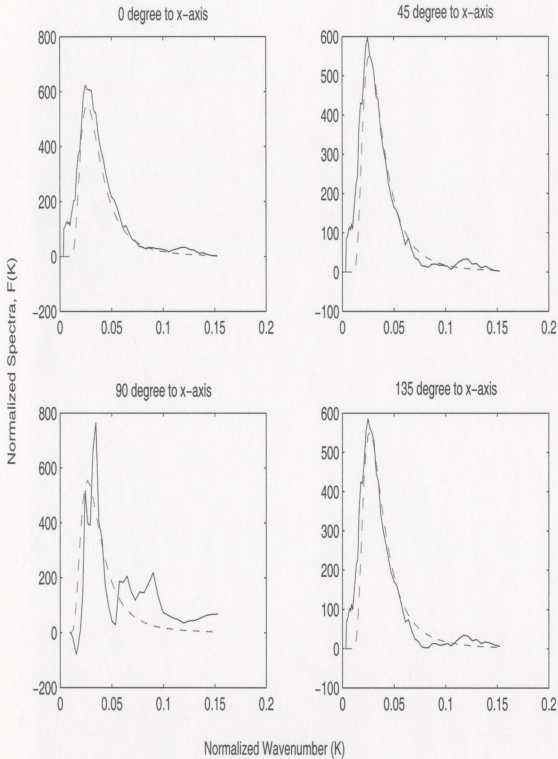


Figure 4.7: The recovered non-directional spectra from noisy radar Doppler PSD for different wind directions. The water is deep, the radar frequency is 25 MHz, and wind speed is 15 m/s. The solid lines are the wave spectra from inversion. The dashed lines are the spectra calculated by Pierson-Moskowitz model.

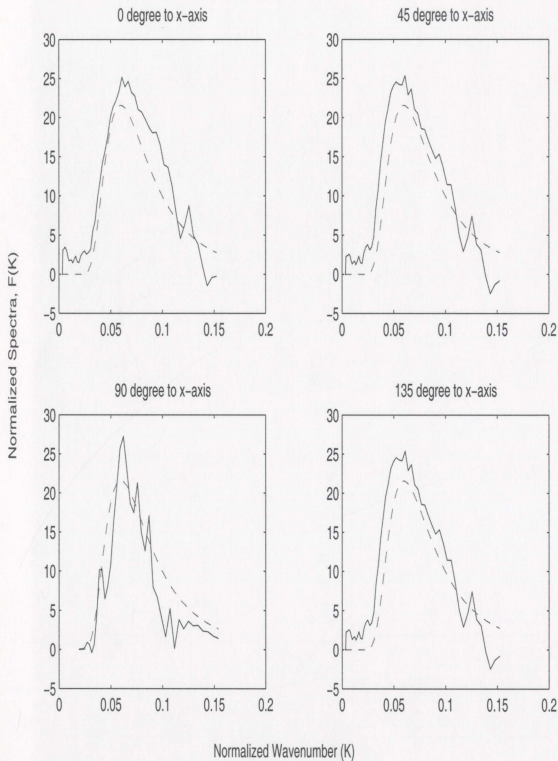


Figure 4.8: The recovered non-directional spectra from noisy radar Doppler PSD for different wind directions. The water is deep, the radar frequency is 25 MHz, and the wind speed is 10 m/s. The solid lines are the wave spectra from inversion. The dashed lines are the spectra calculated by Pierson-Moskowitz model.

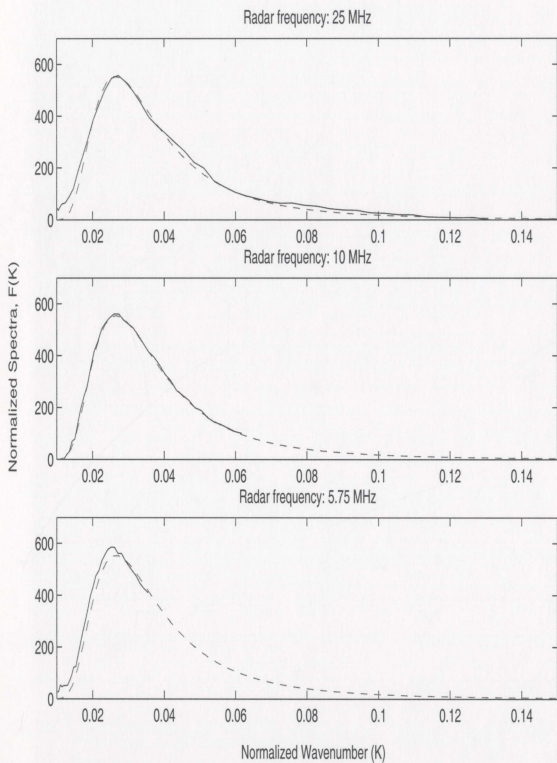


Figure 4.9: The recovered non-directional spectra from noisy radar Doppler PSD for different radar frequencies. The wind speed is 15 m/s, wind direction is  $0^\circ$  to  $x$ -axis, bistatic angle is  $30^\circ$ , and the water is deep. The solid lines are the wave spectra from inversion. The dashed lines are the spectra calculated by Pierson-Moskowitz model.

<i>Depths (m)</i>	<i>Model</i>	<i>Inversion</i>	<i>%Difference</i>
100 (deep)	0.8422	0.8586	1.9
10	0.8426	0.8057	4.4
5	0.8368	0.8776	4.9

Table 4.1: Normalized Waveheights for Different Water Depths.

<i>Directions (degree)</i>	<i>Model</i>	<i>Inversion</i>	<i>%Difference</i>
0	0.8404	0.9495	13.0
45	0.8404	0.8588	2.2
90	0.8404	1.1409	35.8
135	0.8404	0.8433	0.3

Table 4.2: Normalized Waveheights for Different Wind Directions ( $\mu = 15$  m/s).

<i>Directions (degree)</i>	<i>Model</i>	<i>Inversion</i>	<i>%Difference</i>
0	0.3271	0.3549	8.5
45	0.3271	0.3368	3.0
90	0.3271	0.2883	11.9
135	0.3271	0.3368	3.0

Table 4.3: Normalized Waveheights for Different Wind Directions ( $\mu = 10$  m/s).

<i>Frequencies (MHz)</i>	<i>Model</i>	<i>Inversion</i>	<i>%Difference</i>
25	0.8477	0.8687	2.5
10	0.8458	0.7172	15.2
5.75	0.8429	0.4958	41.2

Table 4.4: Normalized Waveheights for Different Radar Frequencies.

# Chapter 5

## Conclusions

### 5.1 General Summary

Based upon bistatic cross sections developed by Gill and Walsh [11], an algorithm has been developed to calculate the non-directional ocean wave spectrum from simulated HF narrow beam bistatic radar returns. The water depth is set to be arbitrary; the current is assumed to be absent. The inverse results for different ocean surface conditions and operating frequencies are considered. Initially, a noise-free signal is assumed.

The second-order cross section of patch scattering, which is one of the dominant features in the radar received data, is normalized by the factor  $2k_0 \cos(\phi_0)$ .

A delta function constraint, appearing in the second-order integrals is solved by means of the Newton-Raphson method. The coupling coefficients and other integrand factors are calculated for each wavenumber.

The inverse scattering analysis refers to the process involved in recovering the ocean wave spectrum from received radar data. Mathematically, it is a problem of solving an integral equation of the first kind. However, the integrand of the second-order cross section equation contains non-linearities resulting from the product of two related factors of ocean wave directional spectra. An approximate linearization suggested by Barrick

and Lipa [16] involving a Phillips equilibrium spectrum [15] is implemented. Also by dividing both sides by the energy inside the first-order peak, the path gains and losses are removed from the second-order cross section.

The discretization of the cross section is accomplished by means of a frequency band approximation and representation of the directional ocean wave spectrum by a truncated Fourier series. The original cross section equation is then converted to a matrix equation in which the Fourier coefficients of the ocean spectrum are the unknowns. Singular value decomposition (SVD) is used to invert the kernel matrix of the equation. Inversion yields the ocean Fourier coefficients and subsequently the results appear in Chapter 3.

In the next step of the research, the power spectral density (PSD) of the Doppler radar receiving power from the ocean scattering patch is simulated with stationary zero-mean Gaussian noise being added. Based on the algorithm in Chapter 3, the inverse analysis is also implemented to recover the non-directional wave spectrum from the simulated noisy data. The results appear in Chapter 4.

The encouraging results show that, even when noise is added, for the upper HF band, (20 to 30 MHz), the linearization method works well, and much of the ocean wave information may be extracted from the HF radars operating in the bistatic mode.

## 5.2 Suggestions for Future Work

Several points may be suggested for future research on the inverse analysis of bistatic scattering in an ocean setting. First, a wide beam HF radar algorithm for the bistatic cross section is suggested. As we have discussed in the previous chapter, the narrow beam HF radar may not give the whole information of ocean surface. Hence we cannot recover the unambiguous wind direction using narrow beam radar data as Gill did in [21] for a wide beam antenna array. However, wide beam operation adds complexity to the inversion problem and, while wind direction may be more readily determined, overall

resolution is obviously decreased.

The ocean surface current is set to be zero in this analysis. This assumption may be removed for future research work to approach the more practical ocean condition. However, as long as the currents are known, their effects can be easily removed from the data.

It has been shown that the bistatic data are still subject to the usual left/right ambiguity problems associated with single radars. Two radar receivers will be better according to the discussion of Howell [20]. Bistatic analysis implies an alternative way to recover the directional information. Consider, for example, that we have a HF radar system with one transmitter and receiver located at one site and another receiver located at another site, distant from the previous. Then, the first system may be operated as a monostatic radar while the transmitter and the other receiver form a bistatic system. The monostatic and bistatic radar cross sections may be obtained simultaneously for a specific ocean patch. The inverse analysis of the two sets of data will give more ocean wave information at a reduced cost compared to that associated with two full radar systems.

Since the HFGWR's already exist at Cape Race and Cape Bonavista, NL and experiments are just now beginning to have these monostatic systems operate in bistatic mode, the models presented in this thesis will be able to be checked against real bistatic radar data.

# Bibliography

- [1] E. Shearman, "Radio science and oceanography," *Radio Science*, vol. 18, no. 3, pp. 299-320, 1983.
- [2] D. Crombie, "Doppler spectrum of sea echo at 13.56 mc./s.," *Nature*, vol. 175, pp. 681-682, 1955.
- [3] Antenna Standards Committee of the IEEE Antennas and Propagation Society, The Institute of Electrical and Electronics Engineers Inc., New York, *IEEE Standard Definitions of Terms for Antennas*, 145-1983 ed., 1983.
- [4] D. Barrick, "First-order theory and analysis of MF/HF/VHF scatter from the sea," *IEEE Transactions on Antennas and Propagation*, vol. 20, pp. 2-10, 1972.
- [5] S. Rice, "Reflection of electromagnetic waves from a slightly rough surface," in *Theory of Electromagnetic Waves* (K. Kline, ed.), pp. 351-378, New York: Interscience, 1951.
- [6] D. Barrick, "Remote sensing of sea state by radar," in *Remote Sensing of the Troposphere* (V. Derr, ed.), ch. 12, pp. 1-46, Washington, DC: U.S. Government Printing Office, 1972.
- [7] D. Barrick and B. Lipa, "The second-order shallow water hydrodynamic coupling coefficient in interpretation of HF radar sea echo," *IEEE J. Oceanic Eng.*, vol. 11, no. 2, pp. 310-315, 1986.

- [8] J. Walsh, "On the theory of electromagnetic propagation across a rough surface and calculations in the VHF region," OEIC Report N00232, Memorial University of Newfoundland, St. John's, Newfoundland, 1980.
- [9] S. Srivastava, *Analysis of HF scattering from an ocean surface: An alternative approach incorporating a dipole source*. PhD thesis, Memorial University of Newfoundland, St. John's, Newfoundland, 1984.
- [10] J. Walsh, R. Howell, and B. Dawe, "Model development for evaluation studies of ground wave radar," Contract Report 90-C14, Centre for Cold Ocean Resources Engineering, 1990. (Prepared for Department of National Defence, Government of Canada, DSS Contract Number W7714-8-5655/01-SS).
- [11] E. Gill and J. Walsh, "High-frequency bistatic cross sections of the ocean surface," *Radio Science*, vol. 36, no. 06, pp. 1459-1475, 2001.
- [12] E. Gill, *The Scattering of High Frequency Electromagnetic Radiation from the Ocean Surface: An Analysis Based on a Bistatic Ground Wave Radar Configuration*. PhD thesis, Memorial University of Newfoundland, St. John's, Newfoundland, 1999.
- [13] D. Barrick, "Extraction of wave parameters from measured HF radar sea-echo doppler spectrum," *Radio Science*, vol. 12, no. 3, pp. 415-424, 1977.
- [14] B. Lipa, "Derivation of directional ocean-wave spectra by integral inversion of second-order radar echoes," *Radio Science*, vol. 12, no. 3, pp. 425-434, 1977.
- [15] O. Phillips, *The Dynamics of the Upper Ocean*. Cambridge, England: Cambridge University Press, 1977.
- [16] B. Lipa and D. Barrick, "Analysis methods for narrow-beam high-frequency radar sea echo," Technical Report ERL 420-WPL 56, National Oceanic and Atmospheric Administration, U.S. Department of Commerce, 1982.

- [17] L. R. Wyatt, "The measurement of the ocean wave directional spectrum from HF radar doppler spectra," *Radio Science*, vol. 21, no. 3, pp. 478-485, 1986.
- [18] L. Wyatt, J. Venn, G. Burrows, A. Ponsford, M. Moorhead, and J. Van Heteren, "HF radar measurements of ocean wave parameters during NURWEC," *IEEE J. Oceanic Eng.*, vol. OE-21, no. 2, pp. 219-234, 1986.
- [19] B. Lipa and D. Barrick, "Extraction of sea state from HF radar sea echo: Mathematical theory and modeling," *Radio Science*, vol. 21, no. 1, pp. 81-100, 1986.
- [20] R. Howell, "An algorithm for the extraction of ocean wave spectra from narrow beam HF radar backscatter," Master's thesis, Memorial University of Newfoundland, St. John's, Newfoundland, 1990.
- [21] E. Gill, "An algorithm for the extraction of ocean wave parameters from wide beam HF radar (CODAR) backscatter," Master's thesis, Memorial University of Newfoundland, St. John's, Newfoundland, 1990.
- [22] D. Barrick and B. Lipa, "A compact transportable HF radar system for directional coastal wavefield measurements," in *Ocean Wave Climate* (M. D. Earle and A. Malahoff, eds.), pp. 153-201, New York: Plenum, 1979.
- [23] E. Gill and J. Walsh, "Extraction of ocean wave parameters from HF backscatter received by a four-element array: Analysis and application," *IEEE J. Oceanic Eng.*, vol. 17, no. 4, pp. 376-386, 1992.
- [24] W. Pierson and L. Moskowitz, "A proposed spectral form for fully developed seas based upon the similarity theory of S.A. Kitaigorodskii," *J. Geophys. Res.*, vol. 69, no. 24, pp. 5181-5190, 1964.
- [25] B. Kinsman, *Wind Waves*. N. J.: Prentice-Hall, 1965.

- [26] K. Hasselmann, "Determination of ocean wave spectra from Doppler return from sea surface," *Nature Physical Science*, vol. 229, pp. 16–17, 1971.
- [27] R. Howell and J. Walsh, "Measurement of ocean wave spectra using narrow beam HF radar," *IEEE J. Oceanic Eng.*, vol. 18, no. 3, pp. 296–305, 1993.
- [28] M. Tucker, *Waves in Ocean Engineering*. New York: Ellis Horwood, 1991.
- [29] The MathWorks, Inc., Natick, Massachusetts, USA, *MATLAB<sup>®</sup> The Language of Technical Computing—Using MATLAB, Version 6*, 2000.
- [30] G. Stewart, *Computer Science and Applied Mathematics*. New York: Academic Press Inc., 1973.
- [31] R. Collin, *Antennas and Radio Wave Propagation*. New York: McGraw-Hill Book Company, 1985.
- [32] B. Dawe, "Radio wave propagation over earth: Field calculations and an implementation of the roughness effect," Master's thesis, Memorial University of Newfoundland, St. John's, Newfoundland, 1988.
- [33] International Telecommunications Union, Geneva, *Propagation in Ionized Media (ITU-R Recommendations, 1994 PI Series Volume )*, 1994.
- [34] W. Pierson, "Wind generated gravity waves," *Advances in Geophysics*, vol. 2, pp. 93–178, 1955.
- [35] P. Bobby, "Estimation of vector surface currents beyond the region of overlap of dual-site HF radar: An implementation of the continuity equation," Master's thesis, Memorial University of Newfoundland, St. John's, Newfoundland, 2003.

# Appendix A

## Computer Programs for Analysis

The algorithm for the inverse scattering analysis is written in *Matlab* [29]. The main program is *MAIN.m* in which the constants and parameters are input and variables are defined. Subroutines, *RadarData.m*, *Attnf.m*, *Noise.m*, *FirstOrder.m*, *FreqBand.m*, and *Matrix.m* are called by *MAIN.m*.

*RadarData.m* is a subroutine in which the radar input data are simulated. The first- and second-order cross sections are calculated according to the description in Chapter 2.

*Attnf.m* is called to calculate the power spectral density (PSD) of radar clutter and to input Gaussian noise.

*Noise.m* is a subroutine program in which the PSD of clutter and noise is converted to the time-domain and added together to form the noisy time series. A *Matlab* [29] *fft* function is used to calculate the PSD of the total radar return.

*FirstOrder.m* is a subroutine used to calculate the energy inside in the first-order peaks. This value is used to normalize the second-order cross section when the inverse analysis is carried out.

*FreqBand.m* subroutine derives the frequency points for inverse analysis.

*Matrix.m* subroutine creates the kernel matrix.

## **% MAIN.m**

**% The main program to invert the noisy spectrum  
% for bistatic second-order cross section  
% for arbitrary water depth**

clear all

### **% Denote the constants**

gg = 9.81; % acceleration due to gravity  
c = 3.0e8; % speed of light  
Alpha = 0.0081;

### **% The coefficients**

u = 15; % wind speed  
f0 = 25e6; % radar wave frequency  
ps = 2000; % patch width  
de = 100; % water depth

### **% Directional angles**

phio = 30\*pi/180; % bistatic angle  
thetaN = 90\*pi/180; % ellipse normal  
thetaw = 0\*pi/180; % wind direction

ro1 = 50000; % from radar transmitter to scattering patch (m)  
ro2 = 50000; % from scattering patch to radar receiver (m)

### **% noise floor**

**% for operating frequency at 25, 10, and 5.75 the Fam are 22, 36, and 42**  
Fam = 22;  
Pnf = -204 + Fam;

### **% Normalizing factors**

k0 = 2\*pi\*f0./c; % radar wavenumber  
normf = 2\*k0\*cos(phio);  
WBp = sqrt(2\*gg\*k0\*cos(phio)\*tanh(2\*k0\*cos(phio)\*de)); % Bragg frequency  
De = de/normf; % normalized water depth

### **% Doppler frequency range**

#### **% zero point is taken off**

dwd = 0.0033\*pi;  
wd1 = -4\*pi:dwd:-1\*dwd;  
wd2 = 1\*dwd:dwd:4\*pi;

wd = [wd1 wd2];

wn=wd./WBp; % normalized frequency

**% the small fraction of thetak1**

dthk1=2.3\*pi/180;

**% RADAR DATA INPUT**

**% radar data without noise**

[cs2pp,wn2]=RadarData(gg,c,Alpha,u,De,f0,phio,thetaN,thetaw,k0,WBp,wn,ps,dthk1,dw  
d);

cs2pb=cs2pp; % without considering the 1<sup>st</sup>-order cross section

wds=wn2;

**% Attnf.m gives the clutter and noise factors**

[PdfN,ppc1]=Attnf(c,ro1,ro2,f0,Fam);

**% Noise.m put noise inside the radar data**

[cs2pc,wdn]=Noise(cs2pb,wds,WBp,ppc1,PdfN);

**% BEGIN THE INVERSE PROCEDURE**

**% the noisy spectrum should be interpolated before inversion**

wnst=interp(wdn,8);

cs2p=interp1(wdn,cs2pc,wnst,'linear');

**% range of wavenumber**

Nb=61;

wl=0.64;

wu=0.95;

[wdt,cs2pt,Wband]=FreqBand(WBp,wnst,cs2p,De,wl,wu,Nb,thetaw);

**% the normalizing and linearizing version of input data**

[wsc1,thw]=FirstOrder(gg,Alpha,u,ps,De,phio,thetaN,thetaw,k0,WBp);

rmn=wsc1;

[PdfN,ppc1]=Attnf(c,ro1,ro2,f0,Fam);

**% the right side of the matrix equation**

cs2pL=cs2pt/ppc1;

**% kernel matrix**

[CC]=Matrix(wdt,Wband,De,ps,gg,u,Alpha,thetaN,thw,dthk1,phio,k0,WBp,rmn);

**% SVD method,**

[U,S,V]=svd(CC,0);

**% check the rounded value and svd**

```

for hh=1:1:length(S(:,1))
    X(hh)=S(hh,hh);
End

```

**% use rank as the truncated number**

```

tr=rank(S);
Sr=S(1:tr,(1:tr));
Ur=U(:,(1:tr));
Vr=V(:,(1:tr));
CP=Vr*inv(Sr)*Ur';

```

**% DERIVE THE WAVE P-M SPECTRUM**

```

wsc=CP*cs2pL';
a0=wsc(1:3:length(wsc));
pmk1=a0';
k1d=Wband(2:length(a0));
pmk2=pmk1(1:length(pmk1)-1);

```

**% the original wave spectrum**

```

km1=k1d;
spma=(0.25*Alpha./(km1.^4)).*exp((-0.74*gg*gg)/(((km1).^2)*(u.^4)));

```

**% the normalized wave spectrum**

```

km2=km1*normf;
spmb=(0.25*Alpha./(km2.^4)).*exp((-0.74*gg*gg)/(((km2).^2)*(u.^4)));

```

**% recover the ocean wave spectrum against the real frequency**

```

diff=spmb-spma;
pmk3=pmk2+diff;

```

**% OUTPUT**

**% plot the selected Doppler frequency points**

```

plot(wnst,10*log10(cs2p),wdt,10*log10(cs2pt),'m*')
figure

```

**% plot the behavior of the singular values**

```

plot(10*log10(X))
figure

```

**% plot the inversion result**

```

plot(km2, spmb, 'r',km2,pmk3,'b')
axis([.01 .15 0 700])
xlabel('Normalized Ocean Wavenumber')
ylabel('Normalized Spectrum')

```

title('f=25MHz, 0 degree to the wind direction, deep water, bistatic')

## **% RadarData.m**

**% The program for simulating the radar received data**

**% subroutine of MAIN.m**

**% Normalized 2nd-order bistatic cross section of patch scatter**

function[cs2pp,wn2]=RadarData(gg,c,Alpha,u,De,f0,phio,thetaN,thetaw,k0,WBp,wn,ps,dthk1,dwd);

csp1=[];

for dd=1:1:length(wn)

**% Range of the cross section and initial guess**

**% k1<k2 only**

if(wn(dd)<-1)

    m1=1;

    m2=1;

elseif ((wn(dd)>=-1)&(wn(dd)<0.))

    m1=-1;

    m2=1;

elseif ((wn(dd)<=1)&(wn(dd)>0.))

    m1=1;

    m2=-1;

else

    m1=-1;

    m2=-1;

end

**% range of the thetak1**

if (abs(wn(dd))>sqrt(2))

    beta1(dd)=acos(2\*(1/wn(dd)).^2);

else

    beta1(dd)=0.;

end

TA1=thetaN-pi:dthk1:thetaN-beta1(dd);

TA2=thetaN+beta1(dd):dthk1:thetaN+pi;

Ba1=beta1(dd);

wnf=wn(dd);

**% TA1 part of the thetak1**

```
TA=TA1;
[csA1]=zoneA(TA,wnf,m1,m2,Ba1,thetaN,thetaw,k0,gg,Alpha,phio,u,De,dthk1);
```

### **% TA2 part of the thetak1**

```
TA=TA2;
[csB1]=zoneB(TA,wnf,m1,m2,Ba1,thetaN,thetaw,k0,gg,Alpha,phio,u,De,dthk1);
```

```
csp11=csA1+csB1;
csp1=[csp1 csp11];
end % end the wd loop
```

### **% factors outside the summation**

```
outf=8*pi*pi;
```

### **% The second-order cross section**

```
cs2pp=outf.*csp1;
wn2=wn;
```

## **% Attnf.m**

### **% calculation of PSD of clutter and noise: Attnf.m**

#### **% subroutine of MAIN.m**

#### **% attenuation factor is calculated by a program in PLATO**

```
function[PdfN,ppc1]=Attnf(c,ro1,ro2,f0,Fam)
L0=c/f0;
```

### **% antenna parameters**

```
tao=13.3e-6; % the pulse width
ttL=333e-6; % the pulse repetition period
NN=24; % number of array elements
ppt=16000; % transmitting power
ggt=1.585; % transmitting gain
ds=L0/2; % space between antenna elements
```

```
BW=2.65*L0/(24*pi*ds); % beam width
ggr=5.48*24*ds/L0; % receiving gain
Ar=0.5*c*tao*ro2*BW; % area of cross section
```

### **% power spectrum density of clutter**

```
du=tao/ttL;
ppc1=L0*L0*du*ppt*ggt*ggr*Ar*(abs(0.55222*0.55222)).^2./(((4*pi).^3)*(ro1*ro2).^2);
```

```

% Power spectrum density of noise
pnc=du*(1.38e-23)*290*(10.^(Fam/10))/2/pi;

md=ceil(-0.5/du);
mu=floor(0.5/du);
pdf1=0;
for i3=md:-1;
    saf1=sin(i3*pi*du)/(i3*pi*du);
    pdf1=pdf1+saf1;
end
pdf2=0;
for i4=1:mu;
    saf2=sin(i4*pi*du)/(i4*pi*du);
    pdf2=pdf2+saf2;
end
PdfN=pnc*(pdf1+pdf2);

```

## **% Noise.m**

```

% calculation of the noisy spectrum
% subroutine of MAIN.m
% we add them together to give the real-like cross section

```

```

function[cs2pc,wdn]=Noise(cs2pb,wds,WBp,ppc1,PdfN)

```

```

% FIX THE INPUT CROSS SECTION DATA

```

```

% add the zero point

```

```

wns1=wds(0.5*length(wds)+1:length(wds));
wns2=wds(1:0.5*length(wds));
wns3=[wns2 0 wns1]; % add a zero in the middle

```

```

% power spectrum density of clutter

```

```

pdfc1=cs2pb(length(cs2pb)*0.5);
pdfc2=cs2pb(0.5*length(cs2pb)+1:length(cs2pb));
pdfc3=cs2pb(1:0.5*length(cs2pb));
pdfc4=[pdfc3 pdfc1 pdfc2]; % add a value in the middle

```

```

% select normalized frequency range from -2 to 2

```

```

wns4=[];
pdfc5=[];
for n1=1:length(wns3)

```

```

tamf1=wns3(n1);
tamc1=pdfc4(n1);
if ((tamf1>=-2)&(tamf1<=2))
    tamf2=tamf1;
    tamc2=tamc1;
    wns4=[wns4 tamf2];
    pdfc5=[pdfc5 tamc2];
end
tamf1=0;
tamc1=0;
end

```

### **% build a 800 points series**

```

dwa=1/800;
wnsa=-1.9:dwa:1.9;
wns=wnsa(2:length(wnsa)-1);

```

### **% interpolate the Doppler spectrum**

```

pdfca = interp1(wns4,pdfc5,wnsa,'linear');
pdfc=pdfca(2:length(pdfca)-1);

```

### **% the spectrum of clutter**

```

PdfC=ppc1.*pdfc;

```

## **% TIME SERIES OF CLUTTER AND NOISE**

```

LT=4096;
Ts=pi/4;
pp=0.5*(length(PdfC)-2);
delF=(wns(3)-wns(1));
for i3=1:LT
    tt=(i3-1)*Ts;
    reCt1=0.;
    imCt1=0.;
    reNt1=0.;
    imNt1=0.;

    for i4=1:pp;
        ran1=rand/WBp;
        reC=cos(wns(2*i4-1)*tt+ran1); % add random phase
        imC=sin(wns(2*i4-1)*tt+ran1);

        ran2=rand/WBp;
        reN=cos(wns(2*i4-1)*tt+ran2);
        imN=sin(wns(2*i4-1)*tt+ran2);
    end
end

```

```

cRoot=sqrt(PdfC(2*i4-1)*delF);
nRoot=sqrt(PdfN*delF);

reCt1=reCt1+reC*cRoot;
imCt1=imCt1+imC*cRoot;
reNt1=reNt1+reN*nRoot;
imNt1=imNt1+imN*nRoot;
end
reCN(i3)=reCt1+reNt1;
imCN(i3)=imCt1+imNt1;
end
cs2pr=reCN;
cs2pi=imCN;

cs2pri=cs2pr+i*cs2pi;

```

## **% PERIODOGRAM GIVES THE NOISY SPECTRUM**

### **% 512 point and 50% overlap**

```

mm=512;
nn=LT/mm;
ffa=0;
for n1=1:nn
    pa1=[];
    nL=mm*(n1-1)+1;
    nU=n1*mm;
    cs2a=cs2pri(nL:nU);

    pa2=fft(cs2a);
    pff1=pa2.*conj(pa2);
    ffa=(ffa+pff1);
end
ffb=0;
for n2=1:nn-1
    pb1=[];
    nS=0.5*(2*n2-1)*mm+1;
    nB=0.5*(2*n2+1)*mm;
    cs2b=cs2pri(nS:nB);

    pb2=fft(cs2b);
    pff2=pb2.*conj(pb2);
    ffb=(ffb+pff2);
end
ffs=(ffa+ffb)/15;

cs2pc1=fftshift(ffs);

```

```
cs2pc=cs2pc1(129:384)/LT;
```

```
% recover the x-axis
```

```
ddw=1/128;
```

```
cs11=-2:ddw:2;
```

```
cs1=cs11(1:512);
```

```
wdn=2*cs1(129:384);
```

## **% FreqBand.m**

```
% Prepare the frequency band of inversion problem.
```

```
% subroutine of MAIN.m
```

```
function[wdt,cs2pt,Wband]=FreqBand(WBp,wnst,cs2p,De,wl,wu,Nb,thetaw)
```

```
% FREQUENCY POINT SELECTION
```

```
wns=wnst;
```

```
ua=1-wu;
```

```
ub=1-wl;
```

```
wdt11=[];
```

```
wdt12=[];
```

```
wdt13=[];
```

```
wdt14=[];
```

```
cs2pt11=[];
```

```
cs2pt12=[];
```

```
cs2pt13=[];
```

```
cs2pt14=[];
```

```
fred1=ua+1;
```

```
fred2=1-ub;
```

```
freu1=ub+1;
```

```
freu2=1-ua;
```

```
% range of the wd and the cross section investigated
```

```
for qq=1:1:length(wns)
```

```
    if ((wns(qq)<=-fred1)&(wns(qq)>=-freu1))
```

```
        wdt1=wns(qq);
```

```
        wdt11=[wdt11 wdt1];
```

```
        cs2pt1=cs2p(qq);
```

```
        cs2pt11=[cs2pt11 cs2pt1];
```

```
    end
```

```

if ((wns(qq)<=-fred2)&(wns(qq)>=-freu2))
    wdt2=wns(qq);
    wdt12=[wdt12 wdt2];
    cs2pt2=cs2p(qq);
    cs2pt12=[cs2pt12 cs2pt2];
end
if ((wns(qq)>=fred2)&(wns(qq)<=freu2))
    wdt3=wns(qq);
    wdt13=[wdt13 wdt3];
    cs2pt3=cs2p(qq);
    cs2pt13=[cs2pt13 cs2pt3];
end
if ((wns(qq)>=fred1)&(wns(qq)<=freu1))
    wdt4=wns(qq);
    wdt14=[wdt14 wdt4];
    cs2pt4=cs2p(qq);
    cs2pt14=[cs2pt14 cs2pt4];
end
end
end

```

#### **% use matrix to convert the elements in array**

```

a=length(wdt11);
A=zeros(a,a);
for n=1:a
    A(n,a-n+1)=1;
end
b=length(wdt13);
B=zeros(b,b);
for m=1:b
    B(m,b-m+1)=1;
end

```

```

u11=wdt11*A;
u21=wdt12;
u31=wdt13*B;
u41=wdt14;

```

```

c11=cs2pt11*A;
c21=cs2pt12;
c31=cs2pt13*B;
c41=cs2pt14;

```

#### **% truncate to the equal length**

```

ns=min([length(u11) length(u21) length(u31) length(u41)]);
u1=u11(1:ns);
u2=u21(1:ns);

```

```
u3=u31(1:ns);
u4=u41(1:ns);
```

```
c1=c11(1:ns);
c2=c21(1:ns);
c3=c31(1:ns);
c4=c41(1:ns);
```

**% rearrangement of the elements in arrays to fit the stable condition**

```
wdt=[];
cs2pt=[];
for r1=1:length(c1)
    if(thetaw==90*pi/180)
        wm11=[u3(r1) u4(r1)];
        csm11=[c3(r1) c4(r1)];
    else
        wm11=[u3(r1) u4(r1) u2(r1) u1(r1)];
        csm11=[c3(r1) c4(r1) c2(r1) c1(r1)];
    end
    wdt=[wdt wm11];
    cs2pt=[cs2pt csm11];
end
```

**% FREQUENCY BAND**

```
ub1=max(abs(wdt))-1;
ua1=1-abs(wdt(1));
```

```
gkl=ua1.*ua1-(ua1.^3);
gku=ub1.*ub1+(ub1.^3);
```

```
wa=sqrt(gkl*tanh(De*gkl))./sqrt(tanh(De));
wb=sqrt(gku*tanh(De*gku))./sqrt(tanh(De));
df=(wb-wa)./Nb;
```

**% the frequency range are divided into equal size fragments**

```
Fb=wa:df:wb;
```

**% derive wavenumber from frequency**

```
[Wband]=Wband1(De,Fb);
```

## **% FirstOrder.m**

**% subroutine of MAIN.m**

**% obtain the wind direction and Fourier coefficient a0**

function[wscl,thw]=FirstOrder(gg,Alpha,u,ps,De,phio,thetaN,thetaw,k0,WBp)

kL=1-.01\*pi/ps/k0;  
kU=1+.01\*pi/ps/k0;  
dk=(kU-kL)/103;  
kds=kL:dk:kU;  
cs12s=[];  
cs22s=[];  
c00=[];  
c01=[];  
c02=[];

for nn=1:length(kds)  
kk=kds(nn);

**% PM spectrum calculation**

spm1 = (0.25\*Alpha./(kk.^4)).\*exp((-0.74\*gg\*gg)/((kk.\*kk)\*(u.^4)));

**% directional factor**

g1 = (4/(3\*pi))\*(cos(0.5\*(thetaN+0.5\*(2)\*pi-thetaw))).^4;  
g2 = (4/(3\*pi))\*(cos(0.5\*(thetaN-thetaw))).^4;

ws1=spm1\*g1;  
ws2=spm1\*g2;

**% Sinc function factor**

sa1 = sinc(ps\*k0.\*(kk-1));  
sa2 = sa1.\*sa1;

**% other factors**

othf = (kk.^2.5)\*ps;  
fL=4\*pi\*pi\*(1+De\*sech(De)\*sech(De)/tanh(De));

**% first-order cross section**

cs11 = (2.^3)\*pi\*k0.\*ws1.\*othf.\*sa2\*fL;  
cs21 = (2.^3)\*pi\*k0.\*ws2.\*othf.\*sa2\*fL;

cs12s =[cs12s cs11];  
cs22s =[cs22s cs21];

fa=(2.^3)\*pi\*k0.\*othf.\*sa2\*fL/2/pi;

ca00=fa;

```

ca11=fa*cos(thetaw);
ca22=fa*cos(2*thetaw);

c00=[c00 ca00];
c01=[c01 ca11];
c02=[c02 ca22];

end
cs12a=(2*sum(cs12s)-(cs12s(1)+cs12s(length(cs12s))))*dk/2;
cs22a=(2*sum(cs22s)-(cs22s(1)+cs22s(length(cs22s))))*dk/2;

% recover the wind direction
% the wind direction cannot be recovered precisely
LtoR=cs22a./cs12a;
root=(LtoR).^0.25;
ta=-1./root;
thw=(thetaN+2*atan(ta));

% recover the Fourier coefficient of a0
ca0=(2*sum(c00)-(c00(1)+c00(length(c00))))*dk/2;
ca1=(2*sum(c01)-(c01(1)+c01(length(c01))))*dk/2;
ca2=(2*sum(c02)-(c02(1)+c02(length(c02))))*dk/2;

B=[cs22a;cs12a];

Ma=[ca0, ca1; ca0, -ca1];

[U,S,V] = svd(Ma,0);
tr=2;
Sr=S((1:tr),(1:tr));
Ur=U(:,(1:tr));
Vr=V(:,(1:tr));

CP=Vr*inv(Sr)*Ur';
wsc1=CP*B;

```

## **% Matrix.m**

**% subroutine of MAIN.m**

**% the main program to create the kernel matrix**

```
function[CC]=Matrix(wdt,Wband,De,ps,gg,u,Alpha,thetaN,thw,dthk1,phio,k0,WBp,rnn)
```

```

CC=[];
for dd=1:1:length(wdt)

    % Range of the cross section and initial guesses
    % k1<k2 only
    if(wdt(dd)<-1)
        m1=1;
        m2=1;
    elseif ((wdt(dd)>=-1)&(wdt(dd)<0.))
        m1=-1;
        m2=1;
    elseif ((wdt(dd)<=1)&(wdt(dd)>0.))
        m1=1;
        m2=-1;
    else
        m1=-1;
        m2=-1;
    end
    LL=m1.*m2;

    beta1(dd)=0.;
    TA1=thetaN-pi:dthk1:thetaN;
    TA2=thetaN:dthk1:thetaN+pi;
    Ba1=beta1(dd);
    wn=wdt(dd);

    % TA1 part of the thetak1
    TA=TA1;

[ccA]=PartA(TA,wn,m1,m2,Ba1,thetaN,thw,k0,gg,Alpha,phio,u,De,dthk1,Wband,rmn);

    % TA2 part of the thetak1
    TA=TA2;

[ccB]=PartB(TA,wn,m1,m2,Ba1,thetaN,thw,k0,gg,Alpha,phio,u,De,dthk1,Wband,rmn);
    CC1=ccA+ccB;
    CC=[CC;CC1];
End

```

## % PartA.m

```

% subroutine for Matrix.m
% TA1 part of the thetak1

```

```
function[ccA]=PartA(TA,wn,m1,m2,Ba1,thetaN,thw,k0,gg,Alpha,phio,u,De,dthk1,Wband,rnn);
```

```
k1b=[];
for ss=1:length(TA);
    Ta=TA(ss);
    [y1,k1,k2,thetak2]=newrph3t(wn,Ta,thetaN,De,m1,m2,Ba1);
    y1a=y1;
    k1a1=k1;
    k2=0;
    thetak2=0;
```

```
% check which band the k1 is belonged to
```

```
k1b1=[];
k1a2=0;
for s1=1:length(Wband)-1
    if((k1a1>Wband(s1))&(k1a1<=Wband(s1+1)))
        k1a2=k1a1;
    else
        k1a2=0.;
    end
    k1b1=[k1b1 k1a2];
end
k1b=[k1b;k1b1];
end
[na nb]=size(k1b);
```

```
ccA=[];
for tt=1:nb % for each frequency band
    for t1=1:na % for each angle
        if(k1b(t1,tt)~=0)
            k1=k1b(t1,tt);
            Ta=TA(t1);
            k2=sqrt(k1.*k1+1-2*k1*cos(Ta-thetaN));
```

```
% thetak2
```

```
beta2=(1+k2*k2-k1*k1)/(2*k2);
if (abs(beta2)<0.001)
    beta2=0.;
elseif(beta2>1.)
    beta2=1.;
elseif(beta2<-1)
    beta2=-1;
end
if((Ta>=thetaN-pi)&(Ta<=thetaN-Ba1))
```

```

    thetak2=thetaN+acos(beta2);
else
    thetak2=thetaN-acos(beta2);
end

```

```

[cc]=joco3(m1,m2,Ta,thetaN,k1,k2,phio,k0,De,thetak2,rmn,thw);

```

### **% Fourier coefficients**

```

cc21(t1)=cc*cos(2*Ta);
cc11(t1)=m1*cc*cos(1*Ta);
cc01(t1)=cc;

```

```

else

```

```

    cc21(t1)=0;
    cc11(t1)=0;
    cc01(t1)=0;

```

```

end % end if loop

```

```

end

```

```

sumcc21=sum(cc21(2:(length(cc21)-1)));
sumcc11=sum(cc11(2:(length(cc11)-1)));
sumcc01=sum(cc01(2:(length(cc01)-1)));

```

```

cc2=(2*sumcc21+0.5*(cc21(1)+cc21(length(cc21))))*dthk1/2;
cc1=(2*sumcc11+0.5*(cc11(1)+cc11(length(cc11))))*dthk1/2;
cc0=(2*sumcc01+0.5*(cc01(1)+cc01(length(cc01))))*dthk1/2;
ccA1=[cc0 cc1 cc2];
ccA=[ccA ccA1];

```

```

end

```

## **% PartB.m**

```

% subroutine for Matrix.m

```

```

% TA2 part of the thetak1

```

```

function[ccB]=PartB(TA,wn,m1,m2,Ba1,thetaN,thw,k0,gg,Alpha,phio,u,De,dthk1,Wband,rmn);

```

```

k1b=[];

```

```

for ss=1:length(TA);

```

```

    Ta=TA(ss);

```

```

    [y1,k1,k2,thetak2]=newrph3t(wn,Ta,thetaN,De,m1,m2,Ba1);

```

```

    y1a=y1;

```

```

    k1a1=k1;

```

```

    k2=0;

```

```

thetak2=0;

% check which band the k1 is belonged to
k1b1=[];
k1a2=0;
for s1=1:length(Wband)-1
    if((k1a1>Wband(s1))&(k1a1<=Wband(s1+1)))
        k1a2=k1a1;
    else
        k1a2=0.;
    end
    k1b1=[k1b1 k1a2];
end
k1b=[k1b;k1b1];
end
[na nb]=size(k1b);

ccB=[];
for tt=1:nb      % for each frequency band
    for t1=1:na  % for each angle
        if(k1b(t1,tt)~=0)
            k1=k1b(t1,tt);
            Ta=TA(t1);
            k2=sqrt(k1.*k1+1-2*k1*cos(Ta-thetaN));

            % thetak2
            beta2=(1+k2*k2-k1*k1)/(2*k2);
            if (abs(beta2)<0.001)
                beta2=0.;
            elseif(beta2>1.)
                beta2=1.;
            elseif(beta2<-1)
                beta2=-1;
            end
            if((Ta>=thetaN-pi)&(Ta<=thetaN-Ba1))
                thetak2=thetaN+acos(beta2);
            else
                thetak2=thetaN-acos(beta2);
            end
        end
    end

[cc]=joco3(m1,m2,Ta,thetaN,k1,k2,phio,k0,De,thetak2,rmn,thw);

% the Fourier coefficients
cc21(t1)=cc*cos(2*Ta);
cc11(t1)=m1*cc*cos(1*Ta);
cc01(t1)=cc;

```

```

else
    cc21(t1)=0;
    cc11(t1)=0;
    cc01(t1)=0;
end % end if loop
end
sumcc21=sum(cc21(2:(length(cc21)-1)));
sumcc11=sum(cc11(2:(length(cc11)-1)));
sumcc01=sum(cc01(2:(length(cc01)-1)));

cc2=(2*sumcc21+0.5*(cc21(1)+cc21(length(cc21))))*dthk1/2;
cc1=(2*sumcc11+0.5*(cc11(1)+cc11(length(cc11))))*dthk1/2;
cc0=(2*sumcc01+0.5*(cc01(1)+cc01(length(cc01))))*dthk1/2;
ccB1=[cc0 cc1 cc2];
ccB=[ccB ccB1];
end

```

## % zoneA.m

**% subroutine for RadarData.m**  
**% TA1 part of the thetak1**

```
function[csA1]=zoneA(TA,wnf,m1,m2,Ba1,thetaN,thetaw,k0,gg,Alpha,phio,u,De,dthk1)
```

```

wn=wnf;
cs2p1=[];
for ss=1:length(TA);
    Ta=TA(ss);
    [y1,k1,k2,thetak2]=newrph3t(wn,Ta,thetaN,De,m1,m2,Ba1);
    LL=m1*m2;

```

**% normalized Jacobian of the transformation**

```
[jocty]=jocty3(y1,k1,k2,De,Ta,thetaN,LL);
```

**% coupling coefficient**

```
[tcc]=tcc3(m1,m2,k1,k2,De,Ta,thetak2,phio,thetaN,k0);
```

**% normalized PM spectrum**

```

spmk1=(0.25*Alpha./(k1.^4)).*exp((-0.74*gg*gg)./(k1.*k1)*(u.^4));
spmk2=(0.25*Alpha./(k2.^4)).*exp((-0.74*gg*gg)./(k2.*k2)*(u.^4));

```

**% directional factor**

```
g1 = (4/(3*pi))*(cos(0.5*(Ta+0.5*(1-m1)*pi-thetaw))).^4;
```

```
g2 = (4/(3*pi))*(cos(0.5*(thetak2+0.5*(1-m2)*pi-thetaw))).^4;
```

```
cs2pA = spmk1*g1*spmk2*g2*tcc*jocty;
```

```
cs2p1=[cs2p1 cs2pA];
```

```
end % end the TA loop for integral by means of thetak1
```

```
% summation gives the cross section
```

```
sumcs2p1=sum(cs2p1(2:(length(cs2p1)-1)));
```

```
if(Ba1==0)
```

```
    csA1=(2*sumcs2p1+0.5*(cs2p1(1)+cs2p1(length(cs2p1))))*dthk1/2;
```

```
else
```

```
    csA1=(2*sumcs2p1+0.5*cs2p1(1)+cs2p1(length(cs2p1))))*dthk1/2;
```

```
end
```

## % zoneB.m

```
% subroutine for RadarData.m
```

```
% TA2 part of the thetak1
```

```
function[csB1]=zoneB(TA,wnf,m1,m2,Ba1,thetaN,thetaw,k0,gg,Alpha,phio,u,De,dthk1)
```

```
wn=wnf;
```

```
cs2p1=[];
```

```
for ss=1:length(TA);
```

```
    Ta=TA(ss);
```

```
    [y1,k1,k2,thetak2]=newrph3t(wn,Ta,thetaN,De,m1,m2,Ba1);
```

```
    LL=m1*m2;
```

```
% normalized Jacobian of the transformation
```

```
[jocty]=jocty3(y1,k1,k2,De,Ta,thetaN,LL);
```

```
% coupling coefficient
```

```
[tcc]=tcc3(m1,m2,k1,k2,De,Ta,thetak2,phio,thetaN,k0);
```

```
% normalized PM spectrum
```

```
spmk1=(0.25*Alpha./(k1.^4)).*exp((-0.74*gg*gg)/((k1.*k1)*(u.^4)));
```

```
spmk2=(0.25*Alpha./(k2.^4)).*exp((-0.74*gg*gg)/((k2.*k2)*(u.^4)));
```

```
% directional factor
```

```
g1 = (4/(3*pi))*(cos(0.5*(Ta+0.5*(1-m1)*pi-thetaw))).^4;
```

```
g2 = (4/(3*pi))*(cos(0.5*(thetak2+0.5*(1-m2)*pi-thetaw))).^4;
```

```

cs2pB = spmk1*g1*spm2*g2*tcc*jocty;
cs2p1=[cs2p1 cs2pB];

end % end the TA loop for integral by means of thetak1

% summation gives the cross section
sumcs2p1=sum(cs2p1(2:(length(cs2p1)-1)));
if(Ba1==0)
    csB1=(2*sumcs2p1+0.5*(cs2p1(1)+cs2p1(length(cs2p1))))*dthk1/2;
else
    csB1=(2*sumcs2p1+cs2p1(1)+0.5*cs2p1(length(cs2p1)))*dthk1/2;
end

```

## % newrph3t.m

**% Newton-Raphson method for shallow water  
% k2 and angle of k2 are obtained**

```
function[y1,k1,k2,thetak2]=newrph3t(wnf,Ta,thetaN,De,m1,m2,Ba1)
```

**% Initial guess**

```

kg=(abs(1-abs(wnf))).^2;
yx1=sqrt(kg);

diff=0.08;
tiny=0.0001;
T=yx1;
while diff>tiny
    if(yx1<0)
        T=-yx1;
    else
        T=yx1;
    end
    X=sqrt(tanh(De*T*T));
    X1=sqrt(tanh(De));
    if(De*T*T>20)
        X2=0;
    else
        X2=T*T*De*(1/cosh(De*T*T)).^2;
    end
    X3=X*X1;
    k2g=sqrt(T.^4+1-2*T*T*cos(Ta-thetaN));
    X5=sqrt(k2g);

```

```

if(T>0.)
    X6=T.^3-T*cos(Ta-thetaN);
else
    X6=-(T.^3-T*cos(Ta-thetaN));
end

X7=sqrt(tanh(De*k2g));

if(De*k2g>80)
    X8=0;
else
    X8=(1/cosh(De*k2g)).^2;
end

GY=wnf+m1*yx1*X/X1+m2*X5*X7/X1;

DERIVG=m1*X/X1+m1*X2/X3+m2*X6*X7/(X1*X5.^3)+m2*X6*X8/(X5*X7*X1);
Y1=yx1-(GY/DERIVG);
diff=abs(Y1-yx1);
yx1=Y1;

end % end 'while' loop
y1=Y1;
k1=y1.*y1;
k2=sqrt(k1.*k1+1-2*k1*cos(Ta-thetaN));

% thetak2
beta2=(1+k2*k2-k1*k1)/(2*k2);
if (abs(beta2)<0.001)
    beta2=0.;
elseif(beta2>1.)
    beta2=1.;
elseif(beta2<-1)
    beta2=-1;
end
if((Ta>=thetaN-pi)&(Ta<=thetaN-Ba1))
    thetak2=thetaN+acos(beta2);
else
    thetak2=thetaN-acos(beta2);
end

```

## **% jocty3.m**

**% the subroutine is for normalized Jacobian of the transformation**

```
function[jocty]=jocty3(y1,k1,k2,De,Ta,thetaN,LL)

k11=sqrt(tanh(k1*De));
if(k1*De<25.)
    k12=k1*De*(1/cosh(De*k1)).^2;
else
    k12=0.;
end
k21=sqrt(tanh(k2*De));
if(k2*De<25)
    k22=k2*De*(1/cosh(De*k2)).^2;
else
    k22=0;
end
yk20=LL*(y1.^3-y1*cos(Ta-thetaN));
Da1=(k11+k12/k11);
Db1=yk20*(k21+k22/k21)/(k2.^1.5);
dgy=(Da1+Db1);
if(dgy~=0)
    joct1=sqrt(tanh(De))/abs(dgy);
else
    joct1=joct1;
end
jocty=(y1.^3)*joct1; % the y.^3 factor is multiplied here
```

## **% tcc3.m**

**% the subroutine to solve coupling coefficient for shallow water**  
**% Gill presented its hydrodynamic at Page 101 in his PhD thesis 1999**

```
function[tcc]=tcc3(m1,m2,k1,k2,De,Ta,thetak2,phio,thetaN,k0)
```

**% ELECTROMAGNETIC COUPLING COEFFICIENTS**

```
k1p2=cos(Ta-thetaN+phio);
k2p2=cos(thetak2+phio-thetaN);
```

```
DE1=k1*(k1-2*k0*k1p2);
DE2=k2*(k2-2*k0*k2p2);
```

```
NE1=(k1*k1p2)*(k2*(k1*cos(Ta-thetak2)-k0*k2p2));
NE2=(k2*k2p2)*(k1*(k2*cos(Ta-thetak2)-k0*k1p2));
```

```
if(DE1<0)
    REALEM1=0;
    IMAGEM1=(NE1/sqrt(-DE1))*((sqrt(-DE1)-k0)/(DE1+k0*k0));
else
    REALEM1=(NE1*k0)/(sqrt(DE1)*(DE1+k0*k0));
    IMAGEM1=NE1/(DE1+k0*k0);
end
```

```
if(DE2<0)
    REALEM2=0;
    IMAGEM2=(NE2/sqrt(-DE2))*((sqrt(-DE2)-k0)/(DE2+k0*k0));
else
    REALEM2=(NE2*k0)/(sqrt(DE2)*(DE2+k0*k0));
    IMAGEM1=NE2/(DE2+k0*k0);
end
```

```
REALEM=0.5*(REALEM1+REALEM2);
IMAGEM=0.5*(IMAGEM1+IMAGEM1);
```

```
emcc=(REALEM+j*IMAGEM)/(2*k0*cos(phi));
```

## % HYDRODYNAMIC COUPLING COEFFICIENTS

```
K1K2=k1*k2*cos(Ta-thetak2);
```

```
ET1=-m1*sqrt(k1*tanh(k1*De))/sqrt(tanh(De));
ET2=-m2*sqrt(k2*tanh(k2*De))/sqrt(tanh(De));
```

```
EAN=(ET1+ET2)/(1-(ET1+ET2).^2);
```

```
K12=k1*k2*tanh(k1*De)*tanh(k2*De);
CON1=ET1*(k2/cosh(k2*De)).^2;
CON2=ET2*(k1/cosh(k1*De)).^2;
EDN=(ET1+ET2)*(K12-K1K2)-0.5*(CON1+CON2);
```

```
EEN=K1K2-ET1*ET2*(ET1.^2+ET2.^2+ET1*ET2)*(tanh(De))^2;
```

```
hcc=(EAN*EDN-0.5*EEN)/(ET1*ET2*tanh(De));
tcc=hcc.*conj(hcc);
% tcc=(emcc+hcc).*conj(emcc+hcc);
```

## **% Wband1.m**

**% the subroutine for the FreqBand.m**  
**% solve the wave bands from dispersion relation**

```
function[Wband]=Wband1(De,Fb);
```

```
Wband0=[];  
for nn=1:length(Fb)  
    if (Fb(nn)<0)  
        m=1;  
    else  
        m=-1;  
    end  
    kx1=Fb(nn).^2; % the initial guess of K  
  
    % Newton-Raphson method for shallow water  
    diff=0.01;  
    tiny=0.0001;  
    kx=kx1;  
    while diff>tiny  
        if(kx1<0)  
            kx=-kx1;  
        else  
            kx=kx1;  
        end  
        gy=Fb(nn)+m*sqrt(kx1.*tanh(kx1.*De))./sqrt(tanh(De));  
        updy=tanh(kx.*De)+kx.*De*(sech(kx*De)).^2;  
        lowdy=sqrt(kx.*tanh(kx.*De)*tanh(De));  
        dgdy=0.5*m*updy./lowdy;  
  
        ky=kx1-gy./dgdy;  
        diff=abs(ky-kx1);  
        kx1=ky;  
    end  
    kk=abs(ky);  
    Wband0=[Wband0 kk];  
end  
Wband=Wband0;
```

# **% joco3.m**

**% subroutine of PartA.m and PartB.m**  
**% Fourier coefficients**

```
function[cc]=joco3(m1,m2,Ta,thetaN,k1,k2,phio,k0,De,thetak2,rmn,thw);
```

```
LL=m1*m2;  
y1=sqrt(k1);
```

**% normalized Jacobian of the transformation**  
[jocty]=jocty3(y1,k1,k2,De,Ta,thetaN,LL);

**% coupling coefficients**  
[tcc]=tcc3(m1,m2,k1,k2,De,Ta,thetak2,phio,thetaN,k0);

```
cc0=2*jocty*tcc/(k2.^4);
```

```
fkB=rmn(1);  
bk0=fkB;  
bk1=m2*fkB*4*cos(thw)/3;  
bk2=fkB*cos(2*thw)/3;
```

```
cc=cc0*(bk0+bk1*cos(thetak2)+bk2*cos(2*thetak2));
```



